A thesis submitted in partial fulfilment of the requirements for the degree of Master of Science (MSc) in

MECHANICAL ENGINEERING

UNIVERSITY COLLEGE LONDON

Decomposition Analysis of Manufacturing and Design Freedom: A Formula Student Case Study

Previous Title: "Design of EV Formula Student Suspension Uprights employing additive manufacturing and topology optimisation"

By

Luis Fernando Sobrino Orihuela

Supervisor: Peter Simpson

Co-Supervisor: Dr. Chu Lun Alex Leung

Department of Mechanical Engineering
UNIVERSITY COLLEGE LONDON

Date of submission: 1st September, 2026

Contents

Nomenclature

Roman symbols

a_x	Longitudinal acceleration
a_y	Lateral acceleration
$c_{x,j}$, $c_{y,j}$, $c_{z,j}$	Influence coefficients, member j
C	Compliance
d_x	Bearing mid-span to load-line offset
D	Cumulative Miner damage
E	Young's modulus
F_{brake}	Brake force at calliper radius
F_{drag}	Aerodynamic drag force
F_x, F_y, F_z	Contact-patch force components
$F_{\text{axial},j}$	Axial force in member j
g	Gravitational acceleration
h	Centre-of-gravity height
H_{outer}, H_{inner}	Bearing longitudinal reactions
l_1	Bearing spacing
l_2	Bearing to wheel-centre offset
l_3, l_4, l_5	Calliper mount geometry
L	Wheelbase
m	Total vehicle mass
m_s, m_{us}	Sprung, unsprung mass
n	Kerb-strike severity factor
R	Corner radius
R_{cal}	Calliper centre-of-area radius
r_R	Rolling radius
SF	Safety factor
T_f, T_r	Front, rear track width
$u_{\max}$	Peak nodal displacement
$\hat{\mathbf{u}}_j$	Unit vector along member j
V	Vehicle speed
V_{outer}, V_{inner}	Bearing vertical reactions
W	Static weight
ΔW_x, ΔW_y	Longitudinal, lateral load transfer
ΔW_{kerb}	Kerb-strike vertical increment
x_{CoG}	Centre-of-gravity longitudinal position

Greek symbols

Γ	Level-set zero contour (surface)
θ	Calliper mount angle
μ_{lat}	Lateral friction coefficient
ν	Poisson's ratio
ρ	Density
σ_y	Yield strength (0.2% proof)
σ_{vM}	von Mises stress
ϕ_{brk}	Brake force distribution
$\phi(\mathbf{x})$	Level-set scalar field
Ω	Solid design domain

Abbreviations

AM	Additive manufacturing
CNC	Computer numerical control
CoG	Centre of gravity
DfAM	Design for additive manufacturing
EV	Electric vehicle
FEA	Finite element analysis
FS	Formula Student
GD	Generative design
IMU	Inertial measurement unit
LCA	Life cycle assessment
LPBF	Laser powder bed fusion
LWBF	Lower wishbone, front
LWBR	Lower wishbone, rear
MSI	Manufacturing Sustainability Insights
TO	Topology optimisation
UTS	Ultimate tensile strength
UWBF	Upper wishbone, front
UWBR	Upper wishbone, rear
YS	Yield strength

List of Figures

List of Tables

Decomposition Analysis of Manufacturing and Design Freedom: A Formula Student Case Study

Luis Fernando Sobrino Orihuela

Department of Mechanical Engineering, University College London

Supervisor: Peter Simpson Co-Supervisor: Dr. Chu Lun Alex Leung

Abstract

Generative design (GD) and additive manufacturing (AM) are routinely evaluated as a single package, conflating the contribution of the design method with the manufacturing freedom that AM provides. No published study has isolated these two variables under matched loading and geometry, so the field lacks a quantitative basis for attributing GD-AM performance gains to either axis. This work separates them through a controlled two-by-two decomposition of a Formula Student rear suspension upright, holding the problem formulation, loads, boundary conditions and material class constant across all variants. Governing load cases were derived from vehicle dynamics first principles, resolved into upright reactions and applied to a generative design study in Autodesk Fusion, with the selected outcome reassessed by finite element analysis in Ansys Mechanical. The GD additive outcome in AlSi10Mg reached 570 g, a 66 % reduction from the machined baseline, while lowering peak von Mises stress at corner exit by 43.1 % and peak deformation by 63.7 %. Of this mass reduction, 91.7 to 97.2 % is attributable to the design method rather than to manufacturing freedom. This split represents an upper bound since the baseline was not previously mass-optimised. When re-solved on a converged mesh against yield strength measured by indentation plastometry on coupons built alongside the component, the solver-reported static initial safety factor of 2.08 fell to 1.60. A 2,500-lap duty cycle derived from vehicle telemetry returned an estimated minimum fatigue safety factor of 1.92. The two axes contribute differently in both magnitude and nature. The design method delivers the majority of the mass savings for a fixed problem statement. Manufacturing freedom's true value lies in enabling the solver's GD output to be built directly, without reinterpretation. However, this benefit depends on strict process control.

Keywords: generative design; additive manufacturing; Formula Student; LPBF; design case study.

1. Introduction

1.1. Background and Motivation

Generative design (GD) is an engineering methodology that uses algorithm-driven software to generate multiple viable structural solutions based on user-defined constraints. Conventionally, design engineers iteratively create a geometry, evaluate it via finite-element analysis (FEA), and manually revise it to meet manufacturing constraints. GD reverses this relationship between problem definition and geometry creation. Instead of starting with a proposed shape and testing its performance, the engineer defines the part's functional boundaries, contact interfaces, obstacles, applied loads, performance targets, and manufacturing constraints. The software then explores the solution space to generate multiple valid candidates. Consequently, the engineer's focus shifts from manually crafting geometry to rigorously specifying requirements and evaluating the software's proposals. In practice, GD augments human capability by surfacing organic, non-intuitive designs; however, it does not replace the need for engineering judgement.

The value of that engineering focus depends on what the design software is optimising for. Structural components in high-performance vehicles face conflicting demands: they must withstand critical service loads while minimising mass. This challenge is particularly pronounced for unsprung components, such as wheels, brakes, and uprights, which the suspension springs do not support. Reducing unsprung mass directly improves suspension responsiveness and tyre contact, increasing mechanical grip across all racing conditions [1].

1.2. Problem Formulation

Generative design tools are often assumed to produce near-optimal components reliably, largely independent of the operator. Practice does not support this claim: the solver only optimises the problem exactly as presented, so the outcome's quality relies entirely on the fidelity of the problem formulation. Peckham *et al.* [2] provide controlled evidence of this dependence. In their study, nine trained engineering teams redesigned an identical component for load-bearing capacity using the same GD software, material, and manufacturing process; the resulting parts differed by approximately 600% in structural load-bearing capacity. The authors concluded that GD shifts engineering judgement from shaping geometry to framing the problem. For the present study, this implies that any meaningful comparison between design approaches requires holding the problem formulation strictly constant. The idealisation of structural loads, definition of spatial boundaries, and specification of constraints must remain identical across all cases, a principle that governs this work's methodology.

The transition from a conventionally machined component to a generatively designed, additively manufactured one is often treated as a single step. In reality, it involves simultaneous changes across three distinct factors: the design method, manufacturing freedom, and material. The material factor is frequently overlooked. Because the range of alloys suitable for laser powder bed fusion (LPBF) is limited, high-strength wrought aluminium alloys like 7075 are prone to solidification cracking [3, 4]. The additive route typically requires AlSi10Mg [5]. This alloy's as-built strength is generally lower than the wrought-tempered equivalents used in machining [5]. Consequently, the benefit of geometric freedom is permanently coupled with a penalty in material properties. Demonstrating that a GD, additively manufactured part can meet stiffness and strength targets at a reduced mass is significant because it proves the geometric advantage can outweigh the material penalty. In applications where higher complexity can be justified by superior performance, such as motorsport, the application of GD and AM to achieve such gains can be more easily justified. GD combined with LPBF has been demonstrated on a suspension component for a Formula Student racing car: a rocker redesigned in Ti6Al4V achieved a 40% mass reduction and three times the load capacity over the original nine-part aluminium assembly, consolidated into a single printed part, and was dynamically validated in-service [6].

1.3. Formula Student

Given Formula Student can resemble a small scale and lean budget motorsport operation, it could be used as a case study for performance and practicality assessment. As an international engineering competition, it challenges university students to design, build, and race a single-seater car that complies with strict technical and safety regulations. UK teams typically operate on a lean budget of £40,000 to £60,000 per season, they rely heavily on industry partners to manufacture specialist components [7]. This financial reality dictates that advanced technologies like additive manufacturing must be both accessible and time-efficient to fit within tight competition schedules. By targeting a mass-critical unsprung component under these constraints, this paper investigates whether GD can be employed beyond geometry creation in a lean-budget setting and provides a realistic case study for wider industry adoption.

1.4. Literature Review

Generative design has matured into production applications across the aerospace and automotive sectors, where lightweighting priorities align closely with those of Formula Student. For example, General Motors used Autodesk Fusion to consolidate an eight-component welded seat-belt bracket into a single additively manufactured part, yielding a structure 40% lighter and 20% stronger than the original [8]. Similarly, Airbus applied this methodology to an A320 cabin partition, achieving a 45% mass reduction that saved roughly 30 kg per aircraft [9]. However, in both cases, the reported benefits stem from combining the design method and the additive manufacturing route, leaving their isolated contributions unknown.

Studies on topology-optimised Formula Student components also report substantial mass savings but share similar methodological limitations. The primary issue is that comparisons typically evaluate entire design–manufacture packages where the design method, manufacturing process, and material all change simultaneously. Consequently, performance improvements cannot be attributed to a single variable. For instance, Herrero [10] applied GD to Formula Student uprights, achieving up to a 39% mass reduction while doubling the safety factor relative to the baseline. Yet, because the study simultaneously introduced LPBF and a switch to Ti-6Al-4V, the specific contributions of the design method, material change, and manufacturing route remain completely entangled. Pastorino [11] explicitly highlights this same confound: comparing an LPBF AlSi10Mg upright against a multi-axis-machined Al-7075-T6 baseline, he concedes that the shift in production process dictates the resulting stiffness, and that the design method's contribution cannot be isolated from manufacturing freedom.

A second major gap is the lack of formal accounting for material data and manufacturing consumption. In the studies above, manufacturing cost is acknowledged only through sponsorship arrangements rather than quantified, and the process energy and build time associated with additive manufacture are not analysed despite their direct relevance to any sustainability assessment [10–12]. Material properties are frequently assumed from literature rather than measured directly, despite the known divergence between as-built LPBF alloys and their wrought counterparts [5]: one Formula SAE study [13] reports that the AlSi10Mg used exhibited roughly 50% lower yield strength than the milled Al-7075 it replaced, but the as-built material properties were not tested.

Finally, the literature lacks physical validation. Most claimed mass reductions rely solely on simulation models of geometries that are never manufactured or tested [14, 15]. Without physical proof, CAD-based mass savings remain theoretical. This thesis addresses this gap by manufacturing the optimised geometry, measuring the as-built material properties on which its safety factors depend, and specifying a strain-gauged validation of the finite-element model for future execution.

1.5. Scope and Objectives

This work aims to quantify the independent contributions of the design method and manufacturing freedom to the mass and structural performance of a Formula Student suspension upright, establishing in the process a replicable workflow for evaluating similar components.

The rear-left upright of the UCL Racing FS26-EV-RL is redesigned within a controlled two-by-two framework that isolates design method (conventional versus generative) from manufacturing freedom (milling-constrained versus additive), directly addressing the confounding of these two variables identified in Section 1.4. The specific objectives, each addressing a limitation established in the preceding sections, are:

1. Derive the governing vehicle load equations acting on the upright from first-principles vehicle dynamics, resolving the loading events (acceleration, braking, cornering, kerb strike, and combined) into upright reactions to create a set of boundary conditions and structural inputs to the GD study.

2. Conduct a GD case study spanning both the milling-constrained and AM-constrained manufacturing routes across a defined shortlist of candidate materials, generating at least one converged candidate solution for each route of the design-method and manufacturing-freedom framework. Shortlisting the most suitable outcome to manufacture.

3. Verify the selected GD candidate by finite-element analysis (FEA) under the governing load cases, targeting a minimum von Mises stress safety factor of $SF \geq 1.5$ and a maximum global stiffness deformation of 0.2 mm.

4. Establish a fatigue-life assessment using an equivalent duty 2,500-lap race distance derived from vehicle telemetry, and check it for methodological consistency against a previously validated case study [11]. Report an estimated design life in kilometers alongside a minimum fatigue safety factor using S-N input data for as-built material properties.

5. Apply design for additive manufacturing (DfAM) principles to select build orientation and support strategy for the chosen candidate, quantifying part mass, support mass (as a proportion of total build mass), and total build time for the LPBF process.

6. Perform and specify physical validation experiments. This involves first measuring the yield strength of samples printed on the same bed as the final component, rather than using literature-assumed material data. Then specify a strain-gauged, scaled test model to validate the finite-element model used in the comparison.

2. Design Envelope

2.1. The Suspension Upright as a Case Study

The upright, or wheel hub carrier, is the structural component in a vehicle's unsprung mass that houses the wheel bearings and brake calliper, and provides the outboard clevis pickup points for the suspension assembly members (Fig. 1). In motion it transmits the road contact-patch forces to the suspension while resisting wheel misalignment that would otherwise alter camber or toe and degrade handling.

The upright was chosen for the complexity of its structural requirements: it must hold suspension geometry under dynamic loads, carry an adequate strength margin under the governing load cases, and minimise mass, since it forms part of the unsprung assembly. The natural frequency of that assembly scales as $\sqrt{k/m_{us}}$, so reducing unsprung mass raises the frequency at which the wheel is returned to the ground: after a kerb strike the tyre spends less time unloaded, preserving grip.

The rear upright in particular was chosen for the team's transition to an electric powertrain. This shift required a new upright independently of this study, providing a component with substantial unexploited mass headroom. The FS24 baseline used for comparison was developed by the UCLRacing team under tight timeline constraints, rather than undergoing a dedicated mass-optimisation exercise. Sized conservatively, it carries no recorded structural failures or measurable deflection in service (Section 4).

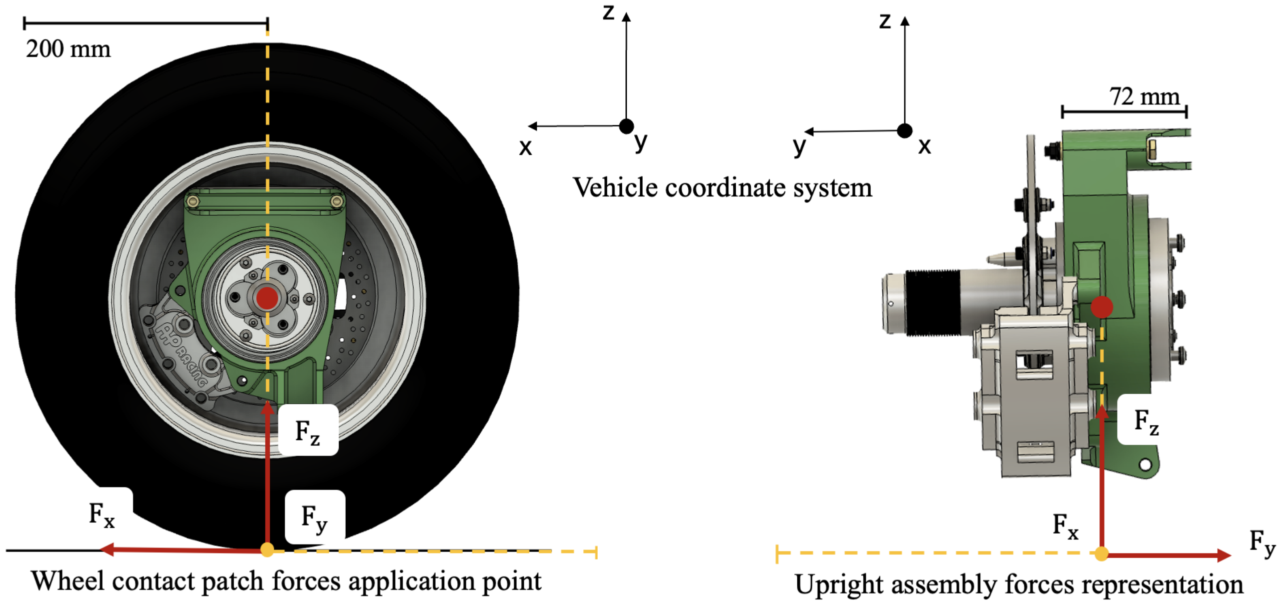

Figure 1: Rear-left upright assembly, contact-patch force application point and the vehicle reference frame used throughout.

Consequently, the mass reduction reported here represents an upper bound on what generative design can recover from an unoptimised conventional part, rather than the margin available against an already optimised one. This context also clarifies the breakdown of the results. The performance gain from manufacturing freedom is fixed, mostly determined by comparing the milling and additively constrained solver outcomes, and is independent of the baseline. Conversely, the gain from the design method scales with the baseline, meaning a leaner starting point would increase manufacturing freedom's relative share.

2.2. Static Vehicle Dynamics

This section outlines the vehicle and wheel loads required for the generative design input parameters and for the static and fatigue of the uprights being analysed. Throughout, forces are expressed in the vehicle reference frame of Fig. 1: origin at the ground plane beneath the front nose, with x longitudinal, y lateral and z vertical (upward positive). The following sections employ vehicle dynamic equations from Milliken and Milliken [1].

Static wheel loads: The total mass is the sum of the driver and the vehicle, and is split into sprung mass m_s, carried by the suspension, and unsprung mass, which includes the wheels, uprights, hubs and the outboard share of the suspension members:

$$W = \left(m_{\text{vehicle}} + m_{\text{driver}}\right) g, \qquad m_s = m - 2\left(m_{us,f} + m_{us,r}\right). \tag{1}$$

Taking moments about the rear axle contact line, the fraction of static weight carried by the front axle depends on the rearward offset of the centre of gravity x_{CoG} from the front axle and the wheelbase L. By lateral symmetry each wheel on an axle carries half its axle load:

$$\%_f = \frac{L - x_{\text{CoG}}}{L}, \qquad W_{\text{wheel},f} = \tfrac{1}{2}\,\%_f\, W, \quad W_{\text{wheel},r} = \tfrac{1}{2}\left(1 - \%_f\right) W. \tag{2}$$

These per-wheel static loads serve as the baseline from which all dynamic force transfers originate.

2.3. Dynamic Load Transfer

Longitudinal load transfer: Taking moments about the front contact line for the inertial couple, the total load shifted between axles is

$$\Delta W_x = m_s\, a_x\, \frac{h}{2L}. \tag{3}$$

Braking is friction-limited: the front wheels gain load and the rear wheels lose it,

$$W_f^{\text{brk}} = W_{\text{wheel},f} + \Delta W_x, \qquad W_r^{\text{brk}} = W_{\text{wheel},r} - \Delta W_x. \tag{4}$$

Under acceleration the transfer reverses in direction: the front wheels lose ΔW_x and the rear driven wheels gain it, so that

$$W_f^{\text{acc}} = W_{\text{wheel},f} - \Delta W_x, \qquad W_r^{\text{acc}} = W_{\text{wheel},r} + \Delta W_x. \tag{5}$$

The force acting at the contact patch is the retarding or driving force per wheel. In braking it is the total retarding force distributed between front and rear; in traction it is the force on the driven axle, limited by the available grip, where ϕ_{brk} is the front/rear brake force distribution.:

$$F_x^{\text{brk}} = \frac{1}{2}\left(m\,a_x + F_{\text{drag}}\right)\phi_{\text{brk}}, \qquad F_x^{\text{acc}} = \frac{1}{2}\,m\,a_x, \tag{6}$$

Lateral load transfer in cornering: Lateral acceleration is calculated from speed and corner radius as $a_y = V^2/R$, capped at the friction limit $\mu_{\text{lat}}\,g$. Lateral transfer is computed separately per axle, since the track width differs front to rear; during a turn the outer wheel gains load and the inner wheel loses it:

$$\begin{aligned} \Delta W_{y,i} &= m_s\,a_y\,\frac{h}{T_i}, \qquad i \in \{f, r\}, \\ W_{RO} &= W_{\text{wheel},r} + \Delta W_{y,r}, \\ W_{RI} &= W_{\text{wheel},r} - \Delta W_{y,r}. \end{aligned} \tag{7}$$

The total lateral force is split front to rear by weight fraction, then between the two wheels of an axle in proportion to their vertical load:

$$F_{y,RO} = F_{c,r}\,\frac{W_{RO}}{W_{RO} + W_{RI}}. \tag{8}$$

A free-body diagram of the vehicle under combined longitudinal and lateral transfer is provided in Appendix A.

Kerb-strike loading: Formula Student events are run on improvised cone-defined circuits within racetracks or airfields, without permanent raised kerbing, so a kerb strike is not an observed racing event but an instant *vertical* shock delivered at the contact patch. It is modelled as a bump load, a multiple of the sprung weight applied vertically, superimposed on the racing condition already in progress. It adds only a vertical component; the longitudinal and lateral tyre forces of the underlying event are unchanged.

The kerb increment is expressed as a factor n of the per-side sprung weight. Taking the sprung weight carried on one side of the car, the vertical load added at one wheel is

$$\Delta W_{\text{kerb}} = n\,\frac{m_s\,g}{2}. \tag{9}$$

Two severities are evaluated: a moderate strike at $2\,g$ and a severe strike at $5\,g$. In each case the increment is added to the vertical wheel load of the base manoeuvre, $W^{\text{kerb}} = W + \Delta W_{\text{kerb}}$, while F_x and F_y are retained unaltered. This overlay is applied to braking, cornering, corner entry and corner exit, producing the $2\,g$ and $5\,g$ variants of each.

2.4. From Contact-Patch Forces to Upright Reactions

The dynamic analysis computed, for each vehicle driving load case, the three tyre force components carried by one wheel at its contact-patch application point: the vertical load F_z, the longitudinal force F_x and the lateral force F_y, expressed in the vehicle frame (Figure 1). These three components constituted the complete input to the upright; every reaction discussed below was resolved from them through the component geometry. The upright carried the vertical load as a bearing force couple across the bearing offset; it carried the longitudinal force both as a bearing couple and, under braking, as a torque reacted at the calliper mounts; and it carried the lateral force as bearing axial thrust together with an additional moment term acting at the rolling radius. Each of the three also contributed to the axial force in every suspension member through its geometric coefficients. The reactions were obtained by treating the upright as a rigid body under each load case, and the same procedure was applied consistently to all cases.

2.5. Governing Load-Case Assembly

A MATLAB (MathWorks, USA) code was developed to derive the full set of governing load cases acting on the upright directly from vehicle dynamics first principles. For each racing event (acceleration, braking, cornering, and combined with kerb strikes), the code resolved the vehicle's mass, weight transfer, and tyre-force limits into twelve load inputs at the upright, returning the force magnitudes that fed directly into both the generative design model and the subsequent finite-element analysis. Two load cases were found to govern the structural requirements, *corner entry* and *corner exit*.

In *corner entry* the vehicle corners while braking bounded by a conservative maximum-grip friction limit of $\mu = 1.2$, combined with the $5\,g$ kerb strike; the rear wheel loses vertical load to forward transfer while gaining lateral transfer to the outside. In *corner exit* the vehicle is on full cornering and peak traction, delivering the instant torque produced by the EMRAX 228 e-motor, again with the $5\,g$ kerb strike, and the rear wheel now gains vertical load through rearward transfer:

$$\begin{aligned} W^{\text{base}} &= W_{\text{wheel},r} + \Delta W_{y,r} + \Delta W_{\text{kerb},5g}, \\ W^{\text{entry}} &= W^{\text{base}} - \Delta W_x, \\ W^{\text{exit}} &= W^{\text{base}} + \Delta W_x, \\ F_x^{\text{entry}} &= -F_x^{\text{brk}}, \qquad F_x^{\text{exit}} = +F_x^{\text{acc}}, \\ F_y^{\text{entry}} &= F_{y,RO}^{\text{brk}}, \qquad F_y^{\text{exit}} = F_{y,RO}^{\text{acc}}, \end{aligned} \tag{10}$$

where W^{base} collects the vertical terms common to both cases and the two manoeuvres are separated only by the direction of longitudinal transfer. Unlike the vertical terms, the lateral reaction is not shared between the two cases. Available grip is friction-limited at each condition (Section 2.3), so the longitudinal force drawn under braking, F_x^{brk}, differs from that drawn under peak traction, F_x^{acc} (Eq. (6)), leaving a different lateral remainder $F_{y,RO}$ once resolved through Eq. (8) at each condition. The transfer terms are taken from Eq. (3) (ΔW_x), Eq. (7) ($\Delta W_{y,r}$) and Eq. (9) ($\Delta W_{\text{kerb},5g}$), and the tyre forces from Eq. (6) and Eq. (8). The negative sign on F_x^{entry} denotes rearward (braking) action; magnitudes are used in the reaction equations of Section 2.6, with sign re-entering only in the applied direction.

2.6. Resolution into Upright Reactions

Bearing reactions: The wheel loads reach the upright through two angular-contact bearings spaced l_1 apart and offset from the wheel-centre plane by l_2 (Fig. 2). The bearing pair reacts the wheel load as a force couple: the vertical and longitudinal forces, applied outboard of the bearing span, load the outer and inner bearings to different magnitudes.

Considering moments about the inner bearing seat, the outer bearing transfers the vertical load amplified by the lever ratio; in any cornering scenario the lateral force F_y, acting at the rolling radius r_R, contributes to the same moment:

$$V_{\text{outer}} = \frac{W\,(l_1 + l_2) + F_y\, r_R}{l_1}, \tag{11}$$

with vertical equilibrium giving the inner reaction:

$$V_{\text{inner}} = V_{\text{outer}} - W. \tag{12}$$

The longitudinal force is reacted similarly, and the lateral force manifests directly as bearing axial thrust:

$$\begin{aligned} H_{\text{outer}} &= \frac{F_x\,(l_1 + l_2)}{l_1}, \\ H_{\text{inner}} &= H_{\text{outer}} - F_x, \qquad F_{y,\text{thrust}} = F_y. \end{aligned} \tag{13}$$

The lever ratio $(l_1 + l_2)/l_1 = 1.34$, together with the rolling-radius term, makes the outer bearing the most heavily loaded location, which is why V_{outer} governs the bearing bore sizing.

Brake-calliper reactions: Under braking the wheel torque is reacted by the calliper; under traction it passes through the hub, so these terms are zero for the corner-exit case. The brake force acts tangentially at the calliper centre-of-area radius and resolves onto the upper and lower mounts through the mount spacing (l_4, l_5) and mount angle θ (Fig. 3):

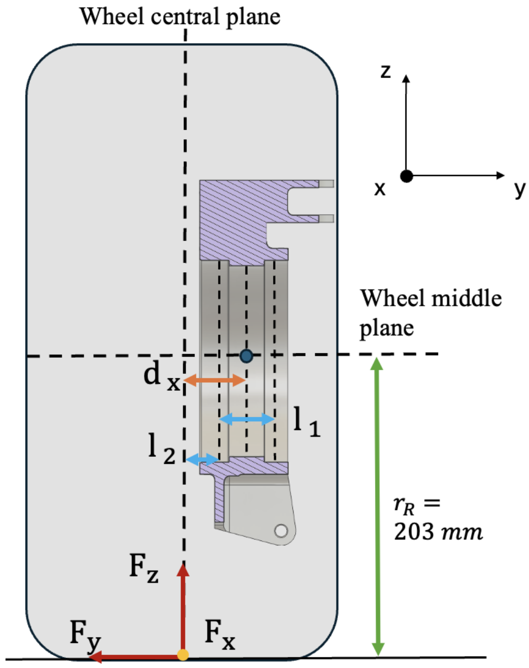

Figure 2: Upright sectioned free-body diagram, showing the bearing spacing l_1, the wheel-centre offset l_2 and the rolling radius r_R.

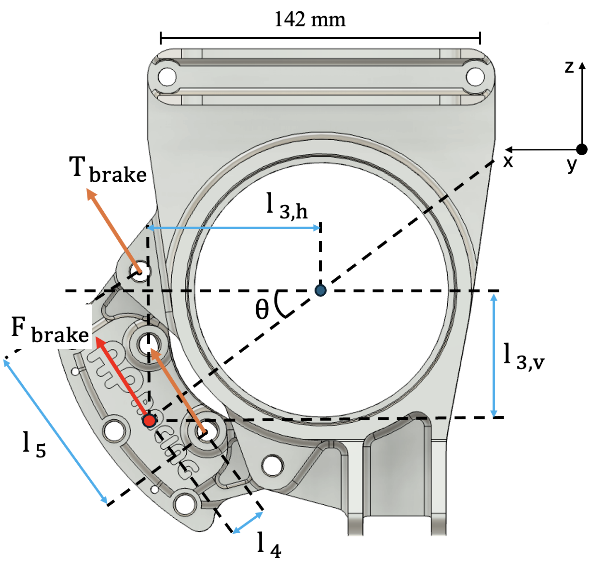

Figure 3: Brake-calliper mount reactions, showing the centre-of-area radius components $l_{3,h}$, $l_{3,v}$, the mount spacing l_4, l_5 and the mount angle θ.

$$\begin{aligned} R_{\text{cal}} &= \sqrt{l_{3,v}^2 + l_{3,h}^2}, \qquad F_{\text{brake}} = \frac{F_x\, r_R}{R_{\text{cal}}}, \\ R_{\text{lwr}} &= F_{\text{brake}}\,\frac{l_4}{l_5}, \qquad R_{\text{upr}} = -\left(F_{\text{brake}} + R_{\text{lwr}}\right), \end{aligned} \tag{14}$$

$$\begin{aligned} V_{\text{brake},j} &= T\cos\theta - R_j \sin\theta, \\ H_{\text{brake},j} &= T\sin\theta + R_j\cos\theta, \qquad j \in \{\text{upr, lwr}\}, \end{aligned} \tag{15}$$

with $T = F_{\text{brake}}/2$. These are the four calliper-mount reactions of Fig. 3.

Suspension link forces: The upright is restrained by six members (two upper-wishbone legs, two lower legs, pushrod and toe rod), each reacting an axial force. These are obtained from the wheel loads using the geometric coefficients $(c_x, c_y, c_z)_j$ generated by the suspension kinematics software LOLA (Lola Cars, UK), which computes the Handford coefficients from the geometric coordinate system on the car:

$$F_{\mathrm{axial},j} = c_{x,j}\, F_x + c_{y,j}\, F_y + c_{z,j}\, W. \tag{16}$$

Each axial force is then resolved along the member's inboard-to-outboard unit vector $\hat{\mathbf{u}}_j$ and applied at the pickup bore centre, the reaction on the upright opposing the member tension. Here $\mathbf{p}_{\mathrm{out},j}$ and $\mathbf{p}_{\mathrm{in},j}$ denote the position vectors of member j's outboard and inboard pickup points respectively, so that $\hat{\mathbf{u}}_j$ points from the inboard mounting on the chassis to the outboard mounting on the upright:

$$\hat{\mathbf{u}}_j = \frac{\mathbf{p}_{\mathrm{out},j} - \mathbf{p}_{\mathrm{in},j}}{\lVert \mathbf{p}_{\mathrm{out},j} - \mathbf{p}_{\mathrm{in},j} \rVert}, \qquad \mathbf{F}_{\mathrm{upright},j} = -F_{\mathrm{axial},j}\, \hat{\mathbf{u}}_j. \tag{17}$$

2.7. Generative Design Input Loads

Applying Eq. (11)–(17) to the two governing manoeuvres yielded the complete reaction sets applied to the generative design model and finite-element comparison of Section 4, listed in Table 1 as individual force components so that each value is traceable to the reaction it represents. Together, these two sets define the structural demand placed on the upright.

To assess whether these magnitudes are physically reasonable, the calculated pushrod force was compared against equivalent Formula Student studies in the literature. Markovits and Szederkényi [6] reported a maximum pushrod force of approximately 9,000 N, and Herrero [10] reported 11,224 N for the same component; the range of 9,084–10,257 N derived in this work lies within this bracket. This agreement supports the validity of the load derivation used here, with the spread across the three studies attributable to differences in vehicle mass, suspension design, and tyre specification between the respective cars.

3. Generative Design Methodology

3.1. Methodology Overview

Structural optimisation aims to develop a component as light as possible while remaining structurally compliant to sustain service loads, by removing or adding material where required, defining an internal load path of the structure, and ensuring those paths connect and move freely as the design improves. This connectivity

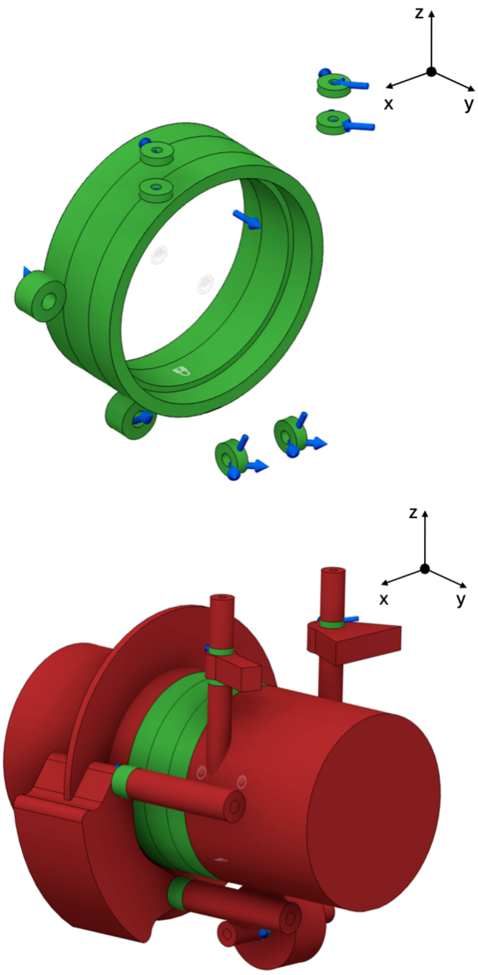

Figure 4: Preserve (top) and obstacle (bottom) geometry.

is defined as a structural topology, and optimising it is referred to as topology optimisation. This study employs the Generative Design (GD) solver in Autodesk Fusion, a cloud-based tool that generates an optimised "outcome" geometry from a set of functional requirements, including allowable build volume, *Preserve* and *Obstacle* bodies, structural loads and manufacturing constraints. In contrast to the traditional design–analysis loop, the solver enables multiple geometry candidates to be assessed simultaneously, depending on the manufacturing and material combination.

3.2. Numerical Mechanism

The Autodesk Fusion GD solver uses a level-set approach to topology optimisation within an allowed space domain [16]. In a level-set formulation, as reviewed by van Dijk *et al.* [17], the solid region Ω of the structure is implicitly represented by a single continuous scalar field $\phi(\mathbf{x})$. This level-set function over point $\mathbf{x}$ of the design space takes a positive value when the point lies within solid material, a negative value if it lies in empty space, and exactly zero on the surface separating the two. The solid part of the structure

Table 1: Generative design input loads, rear-left upright.

Reaction	Symbol	Corner entry (N)	Corner exit (N)	Source
Outer bearing, vertical	$V_{\text{outer},b}$	15108	22185	Eq. (11)
Inner bearing, vertical	$V_{\text{inner},b}$	7685	13990	Eq. (12)
Outer bearing, longitudinal	$H_{\text{outer},b}$	788	1187	Eq. (13)
Inner bearing, longitudinal	$H_{\text{inner},b}$	201	303	Eq. (13)
Bearing axial thrust	F_y	885	1926	Eq. (13)
Upper calliper, vertical	$V_{\text{brake,upr}}$	1544	0	Eq. (15)
Upper calliper, longitudinal	$H_{\text{brake,upr}}$	−1224	0	Eq. (15)
Lower calliper, vertical	$V_{\text{brake,lwr}}$	437	0	Eq. (15)
Lower calliper, longitudinal	$H_{\text{brake,lwr}}$	693	0	Eq. (15)
Upper wishbone, front (UWBF)	F_{axial}	-2176	-3752	Eq. (16)
Upper wishbone, rear (UWBR)	F_{axial}	-1190	-276	Eq. (16)
Lower wishbone, front (LWBF)	F_{axial}	5426	9469	Eq. (16)
Lower wishbone, rear (LWBR)	F_{axial}	3261	1833	Eq. (16)
Pushrod	F_{axial}	-9084	-10257	Eq. (16)
Toe rod	F_{axial}	-583	-618	Eq. (16)

is then the collection of points at which the field is positive, and the physical surface Γ becomes the set of points at which the field passes through zero:

$$\Omega = \{\mathbf{x} : \phi(\mathbf{x}) > 0\}, \qquad \Gamma = \partial\Omega = \{\mathbf{x} : \phi(\mathbf{x}) = 0\}. \tag{18}$$

In essence, the solver operates through an iterative cycle. It merges the current shape and performs a finite-element analysis based on the given loads. In regions where stresses indicate minimal load-bearing, the field is slightly reduced, causing the surface to retract. Conversely, in areas with significant load, the field is maintained or increased, leading the surface to expand. This process gradually shapes the structure to align with the actual load paths, continuing until no more material can be safely removed without violating safety factors, stiffness, or manufacturing constraints.

3.3. Preserve and Obstacle Geometry

The design domain is bounded by two geometric categories. *Preserve* bodies (shown in green in Fig. 4) are the starting positions for the generative design solver and are regions that must be retained for mounting the upright, remaining unaltered during structural optimisation. For the rear upright of a Formula Student car, the *Preserve* geometries are the wheel bearing bore, the suspension members' clevis mounting interfaces and the brake calliper mount holes. *Obstacle* geometries define a design space in which no material may be present, as it would obstruct an existing member's range of motion or an existing interface, including the rim, brake disc and suspension link arms throughout their full range of motion.

3.4. Structural Loads and Boundary Conditions

The structural load inputs from the two governing vehicle conditions formulated in Section 2.5 are transferred onto the preserved geometries' faces. The two governing cases are corner entry (combined braking with the 5 g kerb strike) and corner exit (peak acceleration from the e-motor with the 5 g kerb strike), which represent a severe driving condition rather than a recorded lap scenario. The complete numerical values of each component load, together with the free-body diagrams from which they are obtained, are given in Table 1.

3.5. Design Criteria

The generative design study was set up with a mass-reduction objective, subject to a minimum von Mises stress safety factor of $SF \geq 1.5$ given the already conservative nature of the case loads, and a stiffness constraint limiting maximum global deformation to 0.2 mm, which preserves suspension kinematic accuracy under service loads and avoids excess toe or camber change that can compromise driving stability and road feel.

3.6. Manufacturing and Material Selection

The generative design case studies were evaluated using three representative LPBF materials: Ti-6Al-4V, AlSi10Mg and AISI 304 stainless steel. The freedom of the three materials enables the solver to create unique design variants for each material and allows a visual and data-representative comparison to select the optimal candidate. Materials for the milling-constrained variant included the original upright baseline material, aluminium 6061, and 7075-T6 as a high-performance alternative. Properties are listed in Table 2.

3.7. Manufacturing Constraint Definitions

The following generative design case study parameters were evaluated to generate the outcomes. Each manufacturing input selection followed Design for Additive Manufacturing (DfAM) considerations and literature recommendations for subtractive processes.

- **Unconstrained.** This outcome represents the theoretical performance ceiling when manufacturability constraints are not considered.
- **Additive (build direction +Y).** The build direction is defined along the +Y axis, and a self-supporting overhang of 45° is employed, following the formulations of Gaynor and Guest [22] and Leary *et al.* [23], to ensure new layers are supported by the layer beneath. Minimum wall thickness is set to 4 mm as a conservative LPBF resolution capacity and for robustness in part handling.
- **Milling, 3-axis (build orientation $X\pm/Y\pm$).** Morris *et al.* [24] describe the method behind Fusion's milling constraints and acknowledge that it primarily targets multi-axis CNC milling. Their guidelines were implemented to deliberately select a large tool diameter (10 mm) to restrict surface curvature radius to no less than the bit radius and to create less complex surfaces.

3.8. Design Outcome Selection

Figure 5 summarises the outcomes from both methods in this generative design case study.

The design–manufacturing decomposition of this work aims to perform an analysis of the benefits each stage provides. The final manufacturing material for the additive outcome was therefore selected to be AlSi10Mg, to closely match the baseline alloy performance (Al 6061), so that any attributable structural performance gains and mass savings can be traced either to the benefits of generative design or to the freedom of additive manufacturing, rather than to materialclass substitution.

3.9. Generative Design Convergence

The development of the mass-reduction design criteria described in Section 3.5 can be visualised through the intermediate design stages of Fig. 6.

3.10. Selected Outcomes

The following figures show the selected outcomes from the complete generative design case study, based on the highest-graded structural performance metrics achieved under each manufacturing constraint, down-selected via a visual inspection process to identify potentially inaccessible manufacturable regions or thin, unsuitable geometry that could risk deforming during assembly.

3.10.1. Additive Manufacturing (LPBF)

The selected additively manufactured optimised outcome in AlSi10Mg reached a converged mass of 570 g after DfAM rework operations (Section 3.11), representing a 66 % mass reduction from the baseline mass of 1672 g. The converged safety factor of 2.08 featured a maximum global displacement of 0.194 mm. This outcome geometry requires a comprehensive FEA reassessment in Section 4, owing to the coarse mesh used in the GD study.

The additive-manufactured (AM) GD outcome has been selected as the physical validation prototype because it offers maximum design freedom to capture the highest mass saving and structural performance compared to baseline. AM's benefit is coupled to creating the organic geometry a GD solver produces, so a conventionally designed part would gain no benefit from being additively rather than conventionally manufactured [5]. The additive manufacturing route selected for the design outcome is LPBF, explained in further detail in Section 3.13.

3.10.2. Milling, Three-Axis

The most suitable three-axis-constrained milling concept converged to 661 g for the 10 mm tooling specification, 16 % heavier than the AM concept's converged mass of 570 g, primarily because three-axis subtractive processes can achieve less complex, thicker three-dimensional surfaces with conservative tooling dimensions in a timely, controlled machining environment. This behaviour is consistent with Langelaar [25], who demonstrates that restricting the admissible set of machining directions, together with the tool geometry, directly governs the redistribution of material in the optimised outcome. The same effect is reported by Morris *et al.* [24], whose experiments show that progressively restricting the milling direction set yields less organic truss geometries.

A further limitation of the GD milling outcomes lies within the converged solution lacking a parametric modelling reference for surfaces, which, when visualised on a technical drawing for manufacturing specification, can lead to a surface topology, such as fillet radii, that requires multiple tool changes in a single pass, further increasing manufacturing complexity and lead times. In contrast, the AM variant is not constrained by the lack of parametric modelling in

Table 2: Candidate material properties by manufacturing route.

Material (condition)	**Route**	ρ (kg m^{-3})	E (GPa)	ν	σ_y, 0.2% (MPa)	UTS (MPa)
Ti-6Al-4V (as-built) [18]	Additive (LPBF)	4430	110	0.34	1050	1200–1270
AlSi10Mg (as-built) [19]	Additive (LPBF)	2670	70	0.33	170–218*	330
Stainless 304L (as-built) [20]	Additive (LPBF)	7900	190	0.29	450–560	550–650
Aluminium 6061-T6 [21]	Wrought (milling)	2700	68.9	0.33	259	310
Aluminium 7075-T6 [21]	Wrought (milling)	2810	71.7	0.33	503	572

*Measured by PIP tests on coupons built alongside the component (Section 5.4); all other values from literature.

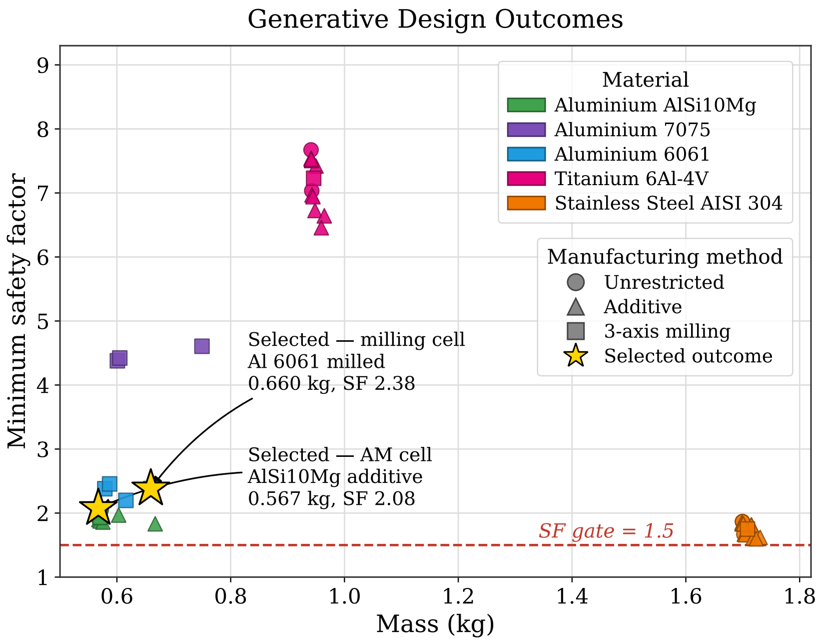

Figure 5: Summary of generative design outcomes across manufacturing definitions.

the organic outcome form, owing to the design freedom of LPBF, as it is not affected by tool access or feature irregularity. The lack of parametric reference features therefore restricts manual reconstruction of a GD outcome to meet suitable subtractive machining standards.

3.10.3. Milling, Five-Axis

For completeness, a supplementary GD study was conducted for a five-axis milling specification at the same tool diameter. The best outcome yielded 601 g, 5.4 % above the AM variant's 570 g, at a minimum safety factor of 2.40 in Al 6061 and a maximum global displacement of 0.2 mm, and achieved a visual similarity to the AM outcome in its organic structure. Morris *et al.* [24] acknowledge that a part satisfying the 5-axis milling constraint may nonetheless be slow to machine, and identify the optimisation of milling time as outstanding future work. No published study appears to have quantified this penalty by machining a generatively designed part and a conventionally designed equivalent. The variant is not carried through to production because it does not serve the decomposition framework: the controlled comparison of Section 1.5 requires a realistically constrained milling baseline for the manufacturing-freedom effect to remain measurable. It shares, in addition, the economic-machinability and non-parametric-surface limitations identified for the three-axis case in Section 3.10.2.

3.10.4. Proposed hybrid approach

Neither additive manufacturing nor multi-axis milling are universally accessible; both carry increased capital cost, lead time and process complexity beyond the reach of many lean-budget teams. A hybrid route is therefore proposed in which the solver outcome is retained as design information rather than as a manufacturing deliverable. The outcome is exported as a mesh and aligned to the existing part on the preserve geometry common to both, and the baseline body is set to reduced opacity so that the study-generated load paths remain visible within the design envelope. Parametric modelling then proceeds outward from the preserves

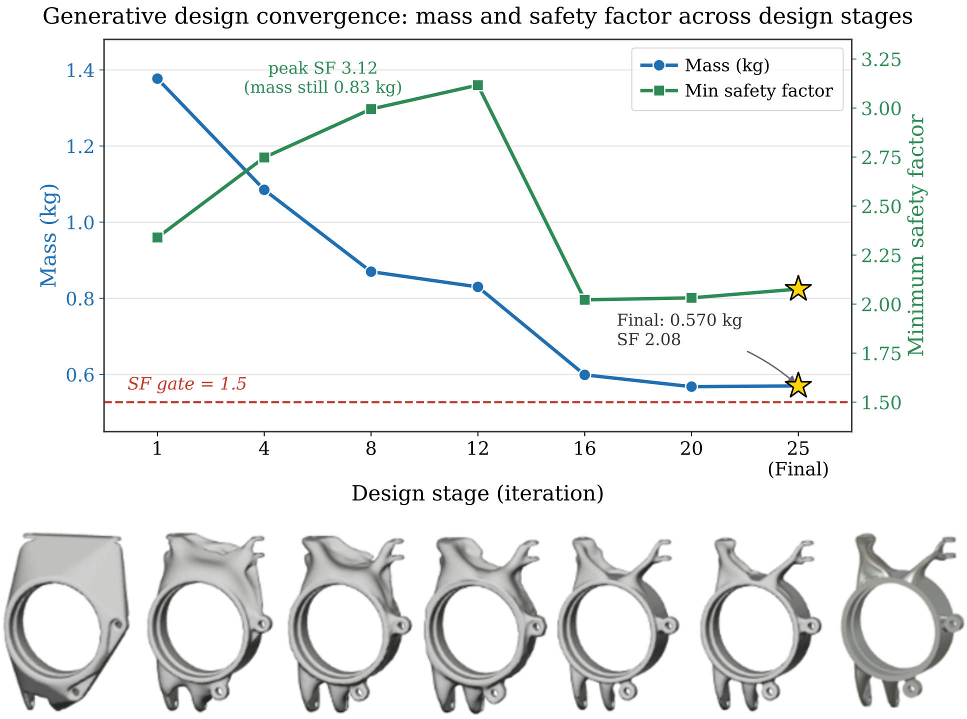

Figure 6: Intermediate design stages and convergence history for the GD AM outcome.

as sketched features placed along those load paths. Because the GD reference is a mesh, it cannot be dimensioned into the timeline, and no non-parametric surface enters the CAD definition, resulting in a fully editable part that can be machined by conventional means. The procedure is set out in Appendix B.

Applied to the rear-left upright, the reconstruction reached 810 g, recovering 78.2 % of the additive mass benefit at a penalty of 240 g against the LPBF outcome. This positions the solver as an instrument for locating structurally compliant load paths on multi-loaded components rather than as a generator of finished geometry, and makes the design-method benefit accessible to a team holding only three-axis capability and a compressed build timeline. The 810 g figure in Table 3 is illustrative and not directly comparable to the software outcomes. The three GD solver outcomes derive from fixed constraints and are repeatable; the hybrid is a manual reconstruction whose mass depends on the load paths retained, the section profiles chosen, and the safety margin left by the engineer. Quantifying the spread across design experience in practitioners remains future work.

3.11. Design for Additive Manufacturing

While additive manufacturing enables maximum design freedom, the final optimised CAD structure still requires manual rework. These implementations shown in Fig. 9 help to: (1) smooth any sharp corners, which is critical to reduce stress concentrations that can produce areas of artificially higher stress zones on FEA, (2) remove any excess material from surfaces, (3) increase the strength of attachments via fillets, and (4) add features such as chamfers on holes. Figure 10 shows a reduction of 37.6 % in von Mises stress resulting from the smoothing of sharp corners that would otherwise produce artificially high stress concentrations in the GD outcome.

3.12. Summary of Performance Across the Design States

The decomposition allows separating confounded variables. The additive achieves a total mass reduction of 1102 g from the baseline. Of this, 91 g (3-axis) and 31 g (5-axis) are due to manufacturing freedom, representing 8.3% and 2.8% of total savings. The remaining 91.7% to 97.2% mainly result from the design method. Based on software alone, the main mass reduction is found to be the computational load-path formulation, not the manufacturing route, regardless of the subtractive specification.

3.13. Additive Manufacturing Process Selection

LPBF was selected on three grounds specific to this geometry and material class. The smallest constrained feature in the design, the upper wishbone clevis bore, measures 3.38 mm at the 70% manufactured scale and was further bounded by a 4 mm minimum-thickness floor in the GD study; LPBF resolves features on the order of 0.5 mm for AlSi10Mg on commercial systems [5, 26], comfortably within

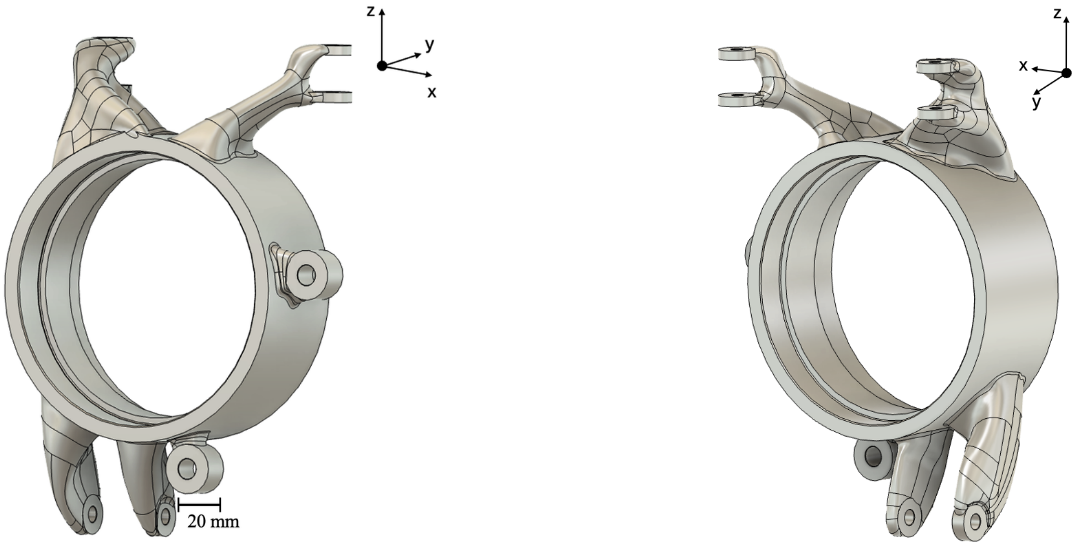

(a) Isometric view. **(b)** Inboard view.

Figure 7: Selected generative design outcome for additive manufacturing in AlSi10Mg.

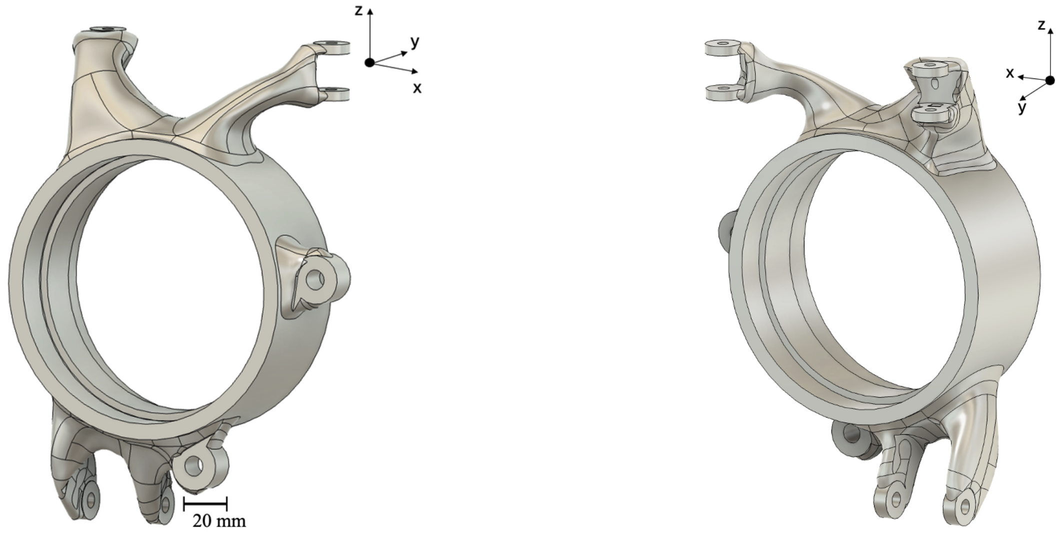

(a) Isometric view. **(b)** Inboard view.

Figure 8: Selected generative design outcome under the 3-axis milling constraint.

this requirement. Material maturity favoured the route, AlSi10Mg has the most extensive aluminium LPBF literature of any candidate alloy, with an established process, published static and fatigue property data, and a documented relationship between processing parameters and porosity [5]. Its dimensional behaviour has also been characterised against the ASME Y14.5 framework [27], giving the geometric deviations reported below a published baseline to be read against. The Henry Royce Discovery Centre at the University of Sheffield manufactured the selected GD outcome on an Aconity3D AconityLAB system (build cylinder ∅170 mm × 200 mm height) in AlSi10Mg. LPBF build process parameters shown in Table 4

4. Finite Element Model

A finite element analysis (FEA) was conducted on both the baseline upright, and the new generative design model created in Section 3, to validate the components' structural performance using the governing case loads were established in Section 2.

4.1. Simulation Setup

Simulations were performed in ANSYS Mechanical (ANSYS Inc., USA) using a linear static structural analysis with tetrahedral elements to capture the complex 3D surface features of the GD outcome. The boundary conditions, applied loads and load case were held identical across all refinement iterations, so that element size remained the independent variable of the

Table 3: Mass, strength and stiffness across the generative design study outcomes.

Design Variant	Mass (g)	Mass saving (%)	Min. SF (–)	Max. disp. (mm)	Share of AM benefit (%)
Conventional milled baseline	1672	—	—	—	—
GD, three-axis milling (Al 6061)	661	60.5	2.38	0.189	91.7
GD, five-axis milling (Al 6061)	601	64.1	2.40	0.200	97.2
GD, additive (AlSi10Mg, LPBF)	570	65.9	2.08	0.194	100.0
Hybrid manual reconstruction	810	51.6	—	—	78.2

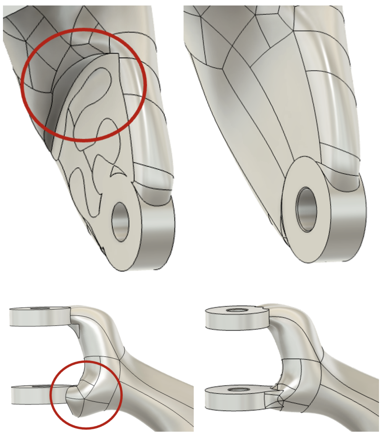

Figure 9: Summary of DfAM rework operations.

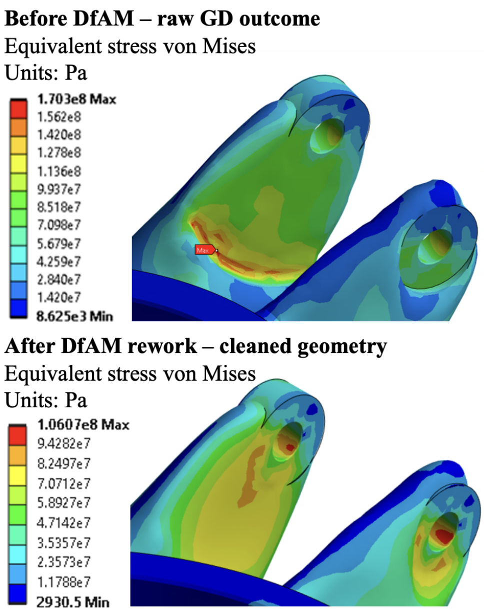

Figure 10: Stress reduction achieved through DfAM.

study. The upright was constrained as a cylindrical support applied to the inner bearing spacer bore, fixing radial, axial, and tangential displacement. This is a conservative simplification of the angular-contact bearing pair but nonetheless compliant. The outer and inner bearing reactions of Table 1 were applied as Bearing Loads. The six suspension-link points were loaded with Remote Force, using rigid behaviour at the bore centre, which represents the axial tension

Table 4: LPBF build process parameters.

Parameter	Value
Laser power	350 W
Layer thickness	30 µm
Scan (hatch) velocity	1133 mm/s
Hatch spacing	0.1 mm (100 µm)
Powder size distribution	15–63 µm

Process parameters after Kumar *et al.* [28]

Table 5: Finite element model settings.

Parameter	**Setting**
Software	ANSYS Mechanical 2024
Analysis type	Linear static structural
Element type	Second-order tetrahedral (SOLID187)
Global element size	8 → 2 mm (study variable)
Local refinement	1 → 0.5 mm at bores, clevises and fillets (study variable)
Maximum skewness	0.9
Smoothing	High
Material	Al 6061 for baseline, AlSi10Mg for GD AM,
Load case	Corner Entry

(+) or compression (-) transmitted through the spherical rod-end bearings used at each physical connection. The brake callipers apply forces to their bore faces. The principal mesh and model settings are summarised in Table 5.

4.2. Mesh Convergence

Establishing a converged mesh is essential to the controlled comparison of this work. The convergence study was carried out under the governing combined load case of cornering, braking and a 5 g kerb strike, representing the complete loading envelope the component is expected to experience. Convergence was defined as a change in peak von Mises stress of less than ± 0.5 % relative to the next-finer mesh.

Six meshes were generated for the baseline geometry

Table 6: Mesh convergence study results.

Mesh	Elem. ($\times10^3$)	Global (mm)	Local (mm)	σ_{vM} (MPa)	Δ (%)
Baseline					
A	90.2	8	1.00	97.07	—
B	151.1	6	0.75	98.01	+0.97
C	232.0	5	0.75	98.89	+0.90
D	317.8	4	0.50	99.58	+0.70
E	378.7	3	0.50	99.04	−0.50
F	649.6	2	0.50	99.26	+0.18
GD AM outcome					
A	44.0	8	1.00	95.90	—
B	91.1	6	0.75	96.39	+0.51
C	158.6	5	0.75	98.04	+1.71
D	188.6	4	0.50	98.81	+0.79
E	217.2	3	0.50	97.97	−0.85
F	311.2	2	0.50	97.57	−0.41
G	478.9	1.5	0.50	97.32	−0.26

by progressively reducing the global and local element sizes; peak von Mises stresses are reported in Table 6. Convergence was reached at mesh E (378.7×10^3 elements, 99.04 MPa), confirmed by a 0.18 % change to the finest mesh F. Mesh E was selected for the baseline. Another convergence study was performed on the GD AM geometry under the same combined load case, given that its organic structure require finer local refinement to resolve peak stress than the baseline. Convergence was reached at mesh F.

4.3. Fatigue Analysis Methodology

4.3.1. Scope and methodology

Fatigue analysis was conducted for the GD AM outcome to quantify whether the part will survive a telemetry-derived duty cycle, given its as-built material endurance limit. This analysis is particularly relevant in the aerospace and automotive industries, where most failures occur [29]. Quantitative studies attribute between 50 and 90 % of all mechanical failures to fatigue rather than static overload [30]. The goal of the fatigue assessment is to evaluate this component's performance and whether it would survive the stated duty cycle.

The duty cycle for validating fatigue life against the FS endurance event is scaled to a 2,500-lap endurance-equivalent duty cycle. By running the fatigue-life analysis on the operational loads combined under a representative modelled lap derived from real telemetry, the findings map onto the methodological framework established by Pastorino [11] for Squadra Corse Politecnico di Torino. However, this methodological similarity does not enable direct safety factor comparison, as the two studies differ in geometry, load derivation, alloy and surface condition; the present assessment retains the as-built surface roughness of the source material fatigue data, whereas the machined baseline does not carry that penalty.

4.3.2. Telemetry and Duty-Cycle Derivation

Duty-cycle regime proportions and per-regime peak load magnitudes were derived from RaceBox chassis-mounted IMU telemetry recorded during a test session (approximately 30 s per lap of continuous data) conducted by UCL Racing at Cranfield Airfield, Bedfordshire. The test was performed on a cone-defined layout set up by the team on the airfield. This cone-defined test surface is representative of the Formula Student endurance event, and the absence of permanent kerb features along the layout explains the zero kerb samples in the recorded telemetry.

The G-force and linear-velocity-derived telemetry data were parsed in MATLAB, where a friction ellipse diagram was plotted to visualise the tyre forces on the a_x vertical axis (positive: accelerating; negative: braking) and the a_y lateral axis (positive: turning left; negative: turning right). This is supported by a plot set of the three forces (F_z, F_y, F_x) to identify the loads the rear-left upright will experience under the friction envelope, filtered with a moving-average filter of 0.6 s delay to remove sensor spikes and general noise. The complete duty cycles at 1000 km are represented in Table 8.

4.3.3. Fatigue Simulation Setup

The ANSYS Mechanical Fatigue Tool was applied to eight static FEA solves, one for each duty-cycle regime. The setup employed a Basquin S–N curve derived from high-cycle fatigue testing of as-built LPBF AlSi10Mg specimens, and tested with their as-built surface roughness intact [31]. This condition is representative of the topology-optimised geometry, whose internal load paths are not mechanically finished; datasets acquired from machined and polished specimens report fatigue strengths higher than those achievable in the as-manufactured condition and would be non-conservative [32, 33]. The full derived dataset is given in Appendix D. Mean stress arising from the vehicle's baseline cruise state was accounted for through a fixed load ratio applied model-wide. The assessment was performed at a single fixed node at the lower clevis outboard leg, selected as the peak-loaded location and retained across all eight regimes so that the accumulated damage describes a single material point. Equivalent von Mises stress at this node was extracted for each regime and the corresponding ratio $R = \sigma_{\text{cruise}}/\sigma_{\text{regime}}$ evaluated. Cruise produced a peak equivalent stress of 16.7 MPa in the component and 10.06 MPa at the critical node. As equivalent

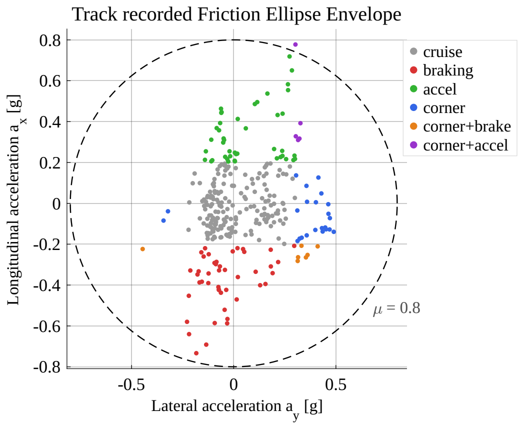

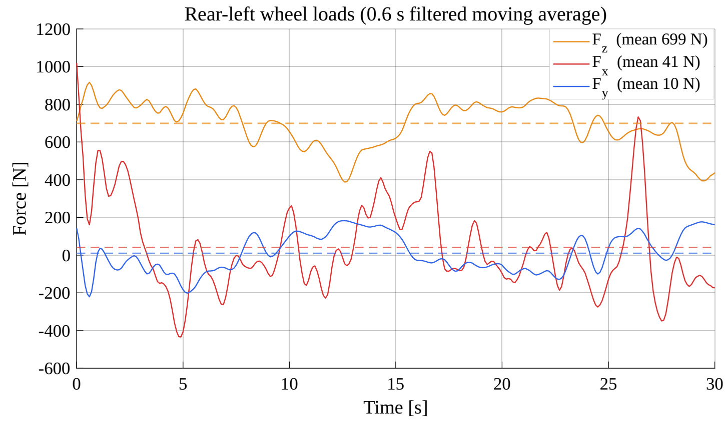

Figure 11: Telemetry-derived friction envelope and force traces from test track session.

stress is unsigned, the load ratios were derived on the basis that the node remains in tension throughout the duty cycle, which the cruise preload arising from the pushrod reaction confirms. Cumulative damage over the 1000 km duty cycle was evaluated by Miner's Damage sum across the eight regimes. A minimum safety factor target was set at ≥ 1.5.

5. Results and Discussion

5.1. Consolidated Governing Case Results

Both uprights were evaluated under the two governing load cases described in Section 2.5: corner entry and corner exit, each combined with a 5 g kerb strike, assuming traction-limited braking grip and peak e-motor acceleration. These conditions are unlikely events in service, so the reported safety factors should be read as assurance under an extreme envelope rather than as service margins. Results are given in Table 7.

At corner entry the GD AM variant matches the baseline in peak von Mises stress (97.57 MPa against 99.04 MPa) while being slightly stiffer (0.080 mm against 0.091 mm), at a 66 % mass reduction. Corner exit showed the largest difference between the designs: peak stress fell 43.1 % from 186.4 MPa to 106.1 MPa, and maximum deformation 63.7 % from 0.457 mm to 0.166 mm. In both variants the peak stress concentration occurs at the lower wishbone clevis, where three members converge and where kerb strike raises both lower wishbone tension and pushrod load; corner exit is the more severe of the two load paths through this joint. The deformation result carries the more direct functional consequence, as upright deflection interferes with camber and toe and therefore with dynamic stability under racing conditions. The two variants are assessed against different materials, 6061-T6 for the machined baseline and as-built AlSi10Mg for the GD AM component, so the safety factor columns are not directly comparable.

Table 7: FEA structural results for governing load cases. Safety factors for the GD AM variant are given as a range spanning the lowest and highest PIP-measured yield strengths (170 MPa to 218 MPa).

Variant	**Max def.** (mm)	**Peak σ_{vM}** (MPa)	**SF**
Corner entry			
Baseline	0.091	99.04	2.62
GD AM	0.080	97.57	1.74–2.23
Corner exit			
Baseline	0.457	186.4	1.39
GD AM	0.166	106.1	1.60–2.05

Safety factors for the GD AM variant span 1.74–2.23 at corner entry and 1.60–2.05 at corner exit, the range reflecting measured variation in material strength rather than a design choice; the lower bound clears the $SF \geq 1.5$ target in both cases. Read against the generative study, however, that lower bound is below the converged minimum safety factor of 2.08 the solver reported for the same outcome, a reduction of 23 %. Two changes separate the values: the refinement from the solver's coarse mesh to the converged model of Section 4.1, and the substitution of measured as-built strength for an assumed value. Only the second is a property of manufacture, and it is the one a subtractive route in a wrought alloy does not carry: yield strength across the coupon population spanned 170 MPa to 218 MPa, a 28 % spread driven principally by build orientation.

Under both load cases the baseline showed no yielding or significant deformation, consistent with its service record of no structural failure or measurable deflection. This confirms that the applied loads, while conservative, sit within a physically acceptable envelope.

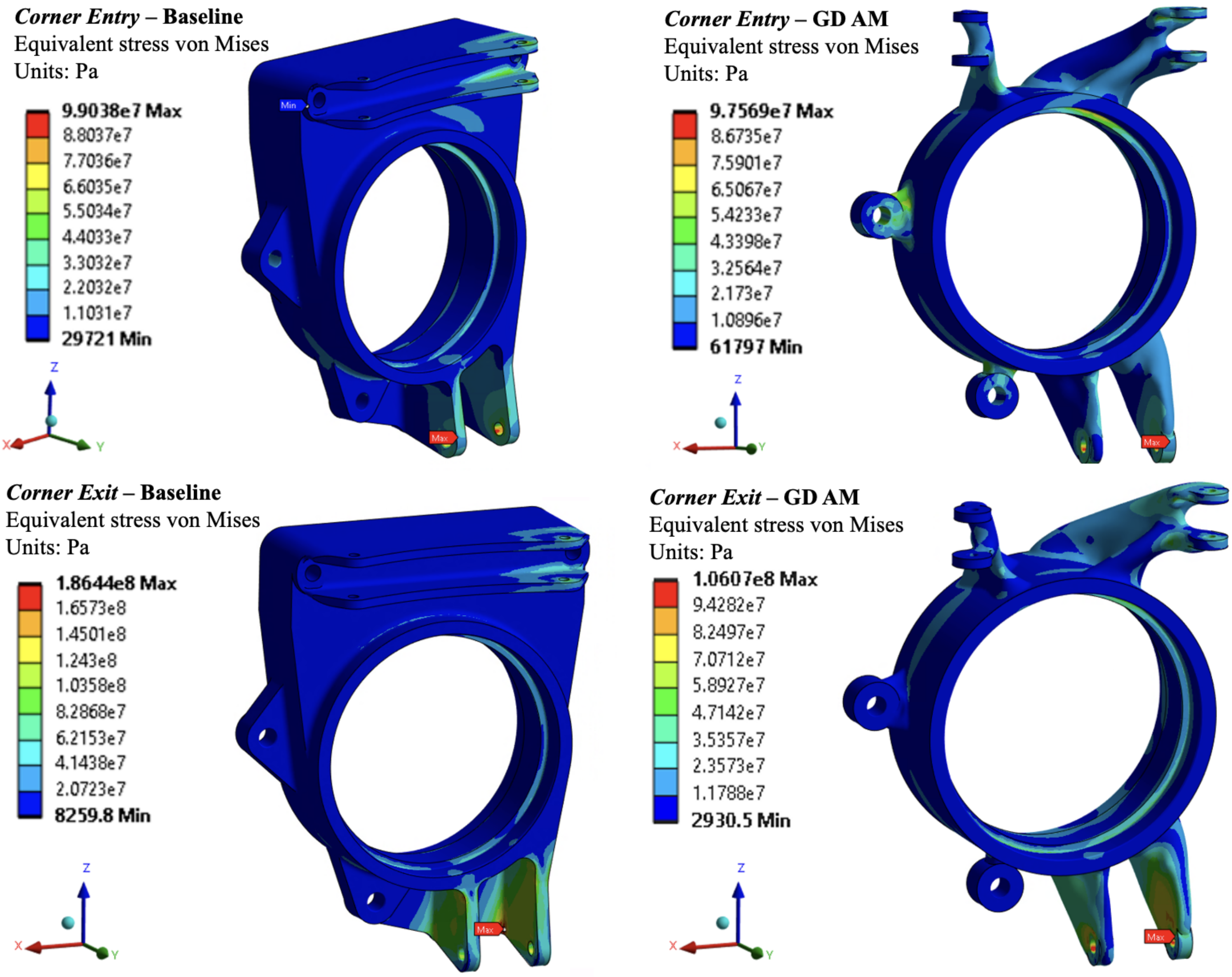

Figure 12: Von Mises stress contours for the governing load cases: corner entry (top row) and corner exit (bottom row).

5.2. Consolidated Fatigue Results

The complete fatigue analysis in the eight load cases, evaluated during the 1000 km duty cycle of Section 4.3.2, produced a total Miner damage of $D = 0.046$, a reserve life factor of approximately 22 relative to that duty cycle, an estimated 21,700 km. Under Miner's linear damage rule the part is not expected to reach fatigue failure within a realistically Formula Student vehicle's service life. All fatigue safety factors remain above the $SF \geq 1.5$ design target, the minimum being 1.92 under the cornering and acceleration case with kerb strike. The combined cornering-and-acceleration regime is the dominant damage contributor (50.5 % of the total), reflecting the coincidence of lateral load with the EV powertrain's instant torque delivery; acceleration in isolation contributes only 4.7 % despite carrying the highest cycle count of any regime. The two kerb-strike regimes together account for 26.5 % of the Miner damage sum and were added as worst-case conservative events not directly tied to recorded telemetry laps. No SF or Damage value is reported for the cruise load case in Table 8, as its stress amplitude of 10.06 MPa falls below the fatigue limit of the material's S-N curve.

The GD AM outcome returns a minimum fatigue safety factor of 1.92, against a minimum of 3.06 reported by Pastorino [11] for a machined Al 7075-T6 upright over a comparable 1000 km endurance duty, a difference of approximately 37 %. Given the confounds identified in Section 4.3 (different geometry, load derivation, alloy and surface condition), this gap cannot be attributed to the manufacturing-freedom axis specifically, it is reported as an indicative comparison against a validated study.

An important caveat is that defect size is the principal parameter controlling the fatigue limit in AM AlSi10Mg [33]. This applies with particular attention to the bearing bores and fastener interfaces, which would be CNC finished for dimensional tolerance and fit; these surfaces are consequently smoother than the as-built condition the S–N data represents, so the analysis would be conservative at those locations. However, the critical node identified here lies on an as-built surface of the optimised structure.

Table 8: Consolidated fatigue results across the eight duty-cycle regimes, evaluated at the lower clevis outboard leg. Global stress is the peak equivalent stress in the component; local stress is at the critical node.

	Duty cycle regime	Global σ_{vm} (MPa)	Local σ_{vm} (MPa)	R	Events per lap	Cycles at 1000 km	Life N_f (cycles)	SF	D
1	Cruise	16.70	10.06	—	19	47,500	—	—	—
2	Braking	60.92	13.96	0.721	10	25,000	3.00×10^7	4.78	0.0008
3	Corner + brake	60.65	25.96	0.388	3	7,500	2.75×10^7	3.68	0.0003
4	Acceleration	62.09	36.22	0.278	11	27,500	1.27×10^7	3.29	0.0022
5	Cornering	85.38	29.11	0.346	6	15,000	2.07×10^6	2.45	0.0073
6	Corner + brake + kerb*	98.79	39.93	0.252	1*	2,500	6.09×10^5	2.35	0.0041
7	Corner + acceleration	95.83	50.94	0.197	4	10,000	4.32×10^5	2.19	0.0231
8	Corner + accel. + kerb*	106.10	90.85	0.111	1*	2,500	3.09×10^5	1.92	0.0081
								Cumulative damage, D_{total}	**0.046**

* assumed worst-case event at one occurrence per lap, not derived from recorded telemetry.

5.3. Additive Manufacture Proof-of-concept

The model was manufactured twice at 70 % of full scale. This scale factor was dictated by the available build envelope, as the full-scale bearing bore diameter of 110 mm, together with the external structure, exceeded the ∅170 mm build cylinder of the AconityLAB. Build data are given in Table 9.

The first build is 2.12 % lighter than the CAD, the second mirrored build, at 188.7 g against the 196.88 g CAD reference, is 4.15 % lighter. Consistent with the as-built findings reported for LPBF AlSi10Mg by Zongo *et al.* [27] and attributable to thermal shrinkage and to the relaxation of residual stress on detachment from the build platform [34]. The support fraction of 3.8 % and 3.4 % of part mass is notably low and provides evidence that the orientation constraint imposed during the GD study produced a genuinely manufacturable outcome rather than one requiring an extensive support strategy. A figure of both parts can be found in Appendix E

Static strain is scale-invariant under geometric similitude, so the model remains as a validation proof for the finite element model. Nevertheless, it is not treated as a geometric qualification of the full-scale component, and the dimensional results must be read as indicative of method rather than predictive of full-scale magnitude. Zongo *et al.* [27] demonstrated experimentally that LPBF AlSi10Mg parts exhibit both intra-part scale effects and inter-part scale effects up to 0.11 mm recorded across three increasing scales of the same artefact. Deviations observed at 70 % scale therefore do not transfer linearly to 100 % scale.

Framed this way, the build converts predicted manufacturability into observed manufacturability, and surfaces the features requiring attention before committing to a full-scale final build.

Table 9: Process and consumable data for both builds.

Quantity	Build 1	Build 2
Part mass (supports removed)	192.7 g	188.7 g
Support mass	7.3 g	6.5 g
Support fraction of part mass	3.8 %	3.4 %
Build time	11.0 h	10.8 h
Argon consumption	2508 L	2440 L
Powder reclaimed	49.0 g	50.7 g

5.4. Material Characterisation (PIP Testing)

The static safety factors reported here depend on as-built AlSi10Mg strength, which was measured directly from specimens printed alongside the analysed component rather than assumed from literature. Profilometry-based indentation plastometry (PIP) recovers the true stress–strain curve by inverse finite-element analysis of a spherical indent profile [35]; Tang *et al.* [36] demonstrated that it reproduces the orientation-dependent response of the columnar, textured microstructures characteristic of as-built LPBF material, which is the governing condition here. Coupons were printed horizontally and vertically on the same platform as the component, isolating build-orientation while sharing its thermal history. Specimens were polished to a P1200 finish on a LaboPol-60 (Struers, Denmark) and tested on a PLX-Benchtop (Plastometrex, UK). Measured properties are given in Table 10. The results spans 170 MPa to 218 MPa in yield strength across builds and orientations, and the static safety factors of Table 7 are reported as a range bounded by these two extremes rather than by a single mean, so that the scatter arising from build orientation is carried into the result rather than averaged out of it. The parts were built on the Vertical (Z) orientation laying down, yet the structure has complex features that remain in the Horizontal (XY) orientation.

Table 10: PIP-measured as-built AlSi10Mg tensile properties by build and coupon orientation.

	Build 1		Build 2	
Property	XY	Z	XY	Z
Yield strength, σ_Y (MPa)	170	218	188	213

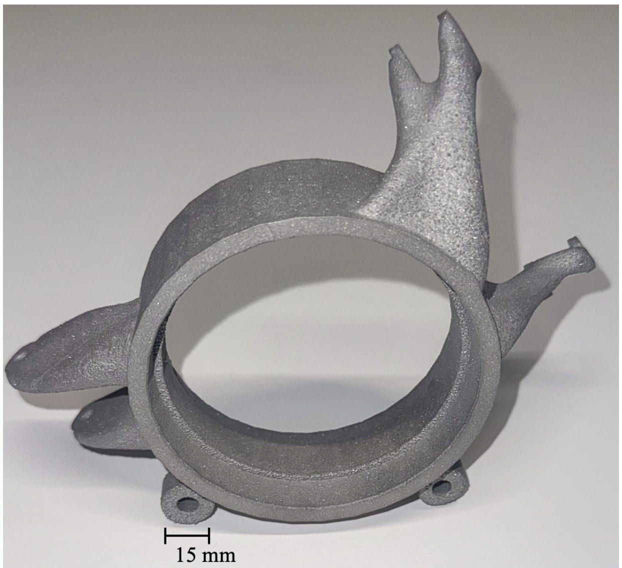

Figure 13: Additively manufactured upright from first build in AlSi10Mg.

5.5. Discussion of Manufactured Results

Two components produced from the same origin geometry, on the same system, and to the same parameters showed measurable geometric distortion concentrated at the calliper mount bore; the manufacturing partner confirmed no known difference between builds. That deviation reflects the process's intrinsic variability. Read alongside the orientation-dependent coupon results, with a mean of 216 MPa in the vertical orientation (Z) against 179 MPa in the horizontal (XY). Both figures sit toward the lower end of the 200–350 MPa range reported across the LPBF AlSi10Mg literature for as-built material [5]. The direction of the orientation split is consistent with the literature results, where the vertical orientation is typically the stronger of the two [37] [38].

The GD carries no representation of thermal history or build parameters. The gap is therefore one of specification rather than execution: the workflow adopted here treated manufacture as a final step due to time constraints and availability, and no dimensional acceptance criteria or in-site monitoring were possible at the point of engagement. The design retained a safety factor above the 1.5 gate across the measured material data, confirming that the geometry itself is structurally adequate; the observed variability reflects production practice, not design validity. For Formula Student teams pursuing sponsored additive manufacture, this implies that dimensional qualification should be scoped as part of the design process itself. This reinforces the central decomposition: the design-method axis delivers the majority of the mass benefit on software, whereas the manufacturing-freedom axis delivers its contribution conditionally, subject to process control that a resource-constrained team may not have access to.

5.6. Manufacturing Sustainability Analysis

A comparative carbon assessment was conducted across the design–manufacturing framework using Manufacturing Sustainability Insights (MSI), a lifecycle module provided within Autodesk Fusion with emission factors from Gravity Climate. The system boundary covers primary raw-material production, inbound transport and manufacturing process energy, with results reported as kg CO_2e per component. Because the tool supplies the emission factors and process proxies rather than this work deriving them, the figures are treated as a directional comparison between routes rather than a certified lifecycle assessment; the system methodology and emission-factor and process assumptions are given in Appendix C.

Total manufacturing emissions fall from 186.30 kg CO_2e for the baseline upright to 23.97 kg CO_2e for the additively manufactured AlSi10Mg outcome, an 87.1 % reduction; however, this narrows to a baseline of 36 kg CO_2e if the stock can be verified as recycled. The two routes, however, shift their impact to different stages. For the milling variants, 97.9 % to 98.1 % of the footprint originates in raw-material production, so generative design yields no meaningful emissions saving on this axis: the billet must still enclose the part's bounding box, and the buy-to-fly ratio of a mass-optimised geometry worsens as more material is removed. For the additive candidate, the impact is dominated instead by raw-material extraction (67.2 %), followed by LPBF processing (31.8 %). This distribution closely matches Weiss *et al.* [39], who attribute the majority of an AM AlSi10Mg part's footprint to aluminium extraction and processing (60.44 % combined) with 35.6 % from LPBF, providing an independent check on the tool's output.

5.7. Environmental Benefit of Lightweighting

The transferable environmental benefit is not based on the manufacturing process itself; rather, it emerges from validating the framework that enables the mass optimisation of structures and the associated environmental advantages of lightweighting, especially within the aerospace industry, where the A320 partition of Section 1.4 remains the reference built example [9]. Huang *et al.* [40] conducted a model of an aircraft fleet and found that approximately 95 % of the projected carbon savings came from reductions in aircraft fuel consumption attributable to lightweighting, with cumulative greenhouse gas savings estimated at 92.8 to 217.4 million tonnes annually.

While lightweighting has demonstrated direct carbon reductions in the aerospace industry, this design case study also provides insights for its application in the automotive industry, enabling indirect carbon savings through downsizing the battery pack of electric vehicles. Alonso *et al.* [41] demonstrated that mass reductions achieved on load-bearing components, most crucially unsprung suspension systems, have the highest potential to decompound gross vehicle mass. Lightweighting across multiple subsystems allows downsizing of the battery pack, the most complex component of an EV, which can reduce the manufacturing greenhouse gas emissions of that component by roughly 8 % with no loss of range [42].

6. Conclusions and Future Work

6.1. Summary of Findings

This work analysed a Formula Student rear upright using a controlled two-by-two decomposition, fixing loads, boundary conditions, and material class to isolate the effects of design method and manufacturing freedom. The key findings are as follows.

- **The design method delivers the mass savings, represented as an upper bound.** Of the 1102 g reduction from the 1672 g baseline, manufacturing freedom accounts for just 91 g (3-axis) down to 31 g (5-axis). As a result, between 91.7 % and 97.2 % of the benefit stems from generative load-path creation alone. The AlSi10Mg design converged in CAD at 570 g (66 % lighter), simultaneously reducing peak corner-exit von Mises stress by 43.1 % and global peak deformation by 63.7 %. This proportional split represents an upper bound for the design method's share of the mass savings (Section 2.1).

- **Manufacturing freedom's value is realising a GD output into a producible part.** The milling study exposed a limit that the mass figures conceal: the solver guarantees only that every surface is reachable by the specified tool, not that the part is economically machinable. GD milling outcomes retained non-parametric surfaces that prevent an editable CAD definition which is impractical in the time and resource limited Formula Student setting. Additive Manufacturing freedom overcomes this barrier.

- **The safety factor a solver reports is not the safety factor of the part.** The generative study returned a converged minimum of 2.08 for the selected outcome; re-solved on a converged mesh against yield strength measured on coupons built alongside the component, the corner-exit minimum falls to 1.60, a reduction of 23 %. Mesh refinement accounts for part of this, but the material substitution is specific to the additive route: coupon yield strength spanned 170 MPa to 218 MPa, a 28 % spread driven principally by build orientation. A team designing a component should aim against measured lower-bound strength in the build orientation actually used.

- **Endurance life was evaluated from test-track data.** A telemetry-derived, 2,500-lap duty cycle returned a Miner damage of $D = 0.046$, and is not expected to reach fatigue failure across a Formula Student design life, with a minimum fatigue safety factor of 1.92 across all eight duty-cycle regimes using as-built material data.

- **Manufacturability was demonstrated, but realised conditionally.** The mirrored builds, produced from one file on one system to one parameter set, differed in geometric distortion at the calliper mount bore, with no setup difference known to the manufacturing partner. The gap remaining is one of specification rather than execution. For teams pursuing sponsored additive manufacture, the practical conclusion is that build parameters and acceptance criteria are design decisions and should be fixed before committing to the build. This completes the decomposition framework established: the design-method axis delivers its benefit based on the geometry in the software, whereas the manufacturing-freedom axis delivers its contribution subject to process control that a resource-constrained team may not hold.

- **Generative design adds value beyond its output geometry.** A hybrid approach was proposed: the raw GD result is used not as a deliverable but as a load-path guideline for manual, parametric reconstruction using conventional milling practice that can be achieved within the manufacturing timeline and lean resources available to a Formula Student team.

- **Environmental value lies in the lightweighting framework**. Predicted manufacturing emissions fell from 186.30 from the milled baseline without recycled content to 23.97 kg CO_2e from the

AM part. The transferable environmental benefit is the validated mass-optimisation workflow, whose payoff is greatest in use-phase-dominated sectors.

When analysed together, the two axes contribute differently in both magnitude and nature. The design method delivers most of the mass savings for a fixed problem statement. Manufacturing freedom's true value lies in enabling the solver's output to be built directly, without reinterpretation. However, this benefit depends on strict process control; this case study showed that the safety factor drops from the solver-reported 2.08 to 1.60 against measured as-built strength. This indicates that component performance relies heavily on material and process-control investments that a lean-budget team must account for. In summary, mass savings stem primarily from the optimisation tool and are largely achievable without additive manufacturing. While additive manufacturing enables direct realisation of the GD component, it comes with notable material and process-control costs.

6.2. Limitations

The additive upright was built and inspected at 70 % scale, set by the build envelope available. Scaled physical models are an established route to validating the assumptions of numerical models where full-scale testing is not achievable [43], and on that basis the built component supports validation of the finite-element model rather than qualification of the full-scale component; closing that gap requires design assurance at full scale. This requirement is highlighted by a second, scale-independent finding: both builds showed measurable geometric distortion at the calliper mount bore, produced under the same nominal parameter set, and the manufacturing partner could attribute no known process difference to it. Two explanations remain open and are not distinguishable from the present data: variability of the LPBF process, which would recur at any scale, or an unmonitored build parameter that a more instrumented engagement might isolate. Because no dimensional acceptance criteria or in-site monitoring were agreed at the point of engagement, this work can establish that the deviation exists but cannot attribute it. The affected bore is a mounting interface which bounds the present finding to assembly fit rather than to the reported safety factors; the 70 %-scale component should accordingly be read as flagging a risk to be instrumented for at full scale, not as evidence that the risk is bounded.

The static results rest on a worst-case governing load case, combining a 5 g kerb strike with cornering. This is a deliberately increased design envelope rather than a measured event, so the reported margins are conservative. Direct instrumentation of the load path, for example, load cells integrated into the pushrod, would assist in verifying measured in-service loads and yield a more representative duty cycle.

The generative milling variant was not physically manufactured. This follows from its impracticality established in Section 3.10.2 and from the machining instrumentation available, but it means the milling and additive routes could not be compared on measured build time and machining effort.

6.3. Future Work

Physical validation of the finite-element model was planned through a sponsorship agreement with Procter and Chester Measurements (PCM), established after the initial project scope was set and therefore carried here as future work. The AlSi10Mg build will first undergo rigorous post-processing to reach the surface finish required for reliable strain gauging (Ra 0.2). PCM will then professionally support the following: the design of bespoke loading fixtures that reproduce realistic suspension load paths within a uniaxial test frame; the installation of three-element strain-gauge rosettes at the predicted stress hotspots, resolving both the magnitude and direction of the principal stresses; and instrumented loading of the part, correlating the measured strains against the FEA predictions to quantify how closely the simulation matches physical behaviour.

A future investigation is proposed to machine the GD milling outcome and record setup count, tool changes and cutting time against the additive build data of Table 9, so that the two manufacturing routes can be compared on lead time, cost and mass.

6.4. Acknowledgments

This work acknowledges the support of the Henry Royce Institute for advanced materials, funded by a grant from the Engineering and Physical Sciences Research Council (EP/R00661X/1). I sincerely thank my supervisor, Peter Simpson, whose continued guidance helped me become a more confident engineer. Special thanks to Dr Alex Leung for his support, who enabled the completion of the physical build. To Luna Jiang, Tom Carson, and Morgan Barnes, for kindly supporting me with the material testing, to the UCLRacing team for providing the vehicle's CAD and telemetry data, and to Jack Chester at PCM for supporting future work. I dedicate this work to my family, whose love and support made this project possible.

Declaration of AI (Category 2). Claude (Anthropic, https://claude.ai/new) was used in an assistive role during the preparation of this thesis, including consistency checks against figures, tables and cross-references, and code formatting/debugging suggestions for MATLAB and LaTeX.

Grammarly (Superhuman Platform Inc, https://app.grammarly.com/) for academic language suggestions in grammar, spelling and style suggestions.

References

[1] William F. Milliken and Douglas L. Milliken. *Race Car Vehicle Dynamics*. SAE International, 1995. ISBN 978-1-56091-526-3.

[2] Oliver Peckham, Christer W. Elverum, Ben Hicks, Mark Goudswaard, Chris Snider, Martin Steinert, and Sindre W. Eikevåg. Investigating and characterizing the systemic variability when using generative design for additive manufacturing. *Applied Sciences*, 14(11):4750, 2024. doi: 10.3390/app14114750.

[3] John H. Martin, Brennan D. Yahata, Jacob M. Hundley, Justin A. Mayer, Tobias A. Schaedler, and Tresa M. Pollock. 3D printing of high-strength aluminium alloys. *Nature*, 549(7672): 365–369, 2017. doi: 10.1038/nature23894.

[4] H. R. Kotadia, G. Gibbons, A. Das, and P. D. Howes. A review of laser powder bed fusion additive manufacturing of aluminium alloys: Microstructure and properties. *Additive Manufacturing*, 46:102155, 2021. doi: 10.1016/j.addma.2021.102155.

[5] Nesma T. Aboulkhair, Marco Simonelli, Luke Parry, Ian Ashcroft, Christopher Tuck, and Richard Hague. 3D printing of aluminium alloys: Additive manufacturing of aluminium alloys using selective laser melting. *Progress in Materials Science*, 106:100578, 2019. doi: 10.1016/j.pmatsci.2019.100578.

[6] Tamás Markovits and Bence Szederkényi. Investigation of generative design for powder bed fusion technology in case of formula student race car components using ti6al4v alloy. *Journal of Manufacturing Processes*, 80:220–231, 2022. doi: 10.1016/j.jmapro.2022.05.058.

[7] Warren Menezes. High stakes in higher education: The true price of UK Formula Student endeavours. The Asterisk, 2024. URL `https://warrenmenezes.substack.com/p/exclusive-uk-formula-student-teams`. Formula Student team expenditure obtained via Freedom of Information requests. Accessed: 2026-08-19.

[8] Autodesk. Lighter, more efficient future of automotive part design at GM. `https://www.autodesk.com/design-make/articles/automotive-design`, 2018. Accessed: 2026-08-19.

[9] Airbus. Pioneering bionic 3D printing. `https://www.airbus.com/en/newsroom/news/2016-03-pioneering-bionic-3d-printing`, 2016. Accessed: 2026-08-19.

[10] Carla Maria Herrero. Development of generative design uprights for the 2023 formula student car. Master's thesis, University College London, Department of Mechanical Engineering, 2023. MECH0020 Individual Project, AY 2022/23.

[11] Riccardo Pastorino. Design of the upright assembly of a formula student prototype. Master's thesis, Politecnico di Torino, 2023. Supervisors: A. Tonoli and S. Favelli.

[12] Jixiong Li, Jianliang Tan, and Jianbin Dong. Lightweight design of front suspension upright of electric formula car based on topology optimization method. *World Electric Vehicle Journal*, 11(1):15, 2020. doi: 10.3390/wevj11010015.

[13] Ondřej Vaverka, Daniel Koutny, and David Paloušek. Topologically optimized axle carrier for Formula Student produced by selective laser melting. *Rapid Prototyping Journal*, 25(9):1545–1551, 2019. doi: 10.1108/RPJ-07-2018-0171.

[14] Harry Bikas, John Stavridis, Panagiotis Stavropoulos, and George Chryssolouris. Design and topology optimization for additively manufactured structural parts: A Formula Student case study. In *6th BETA CAE International Conference*, 2018.

[15] Tudor-Flavius Zach and Mircea-Cristian Dudescu. The topological optimization and the design for additive manufacturing of a steering knuckle for Formula SAE electric vehicle. *MATEC Web of Conferences*, 343:04011, 2021. doi: 10.1051/matecconf/202134304011.

[16] Autodesk. Introduction to generative design. Autodesk University, 2020.

[17] N. P. van Dijk, K. Maute, M. Langelaar, and F. van Keulen. Level-set methods for structural topology optimization: a review. *Structural and Multidisciplinary Optimization*, 48(3):437–472, 2013.

[18] F. Bartolomeu, M. Gasik, F. S. Silva, and G. Miranda. Mechanical properties of Ti6Al4V fabricated by laser powder bed fusion: a review focused on the processing and microstructural parameters influence on the final properties. *Metals*, 12(6):986, 2022. doi: 10.3390/met12060986.

[19] N. T. Aboulkhair, M. Simonelli, L. Parry, I. Ashcroft, C. Tuck, and R. Hague. 3d printing of aluminium alloys: additive manufacturing of aluminium alloys using selective laser melting. *Progress in Materials Science*, 106:100578, 2019. doi: 10.1016/j.pmatsci.2019.100578.

[20] Milad Ghayoor, Kijoon Lee, Yujuan He, Chih-Hung Chang, Brian K. Paul, and Somayeh Pasebani. Selective laser melting of 304l stainless steel: role of volumetric energy density on the microstructure, texture and mechanical properties. *Additive Manufacturing*, 32:101011, 2020. doi: 10.1016/j.addma.2019.101011.

[21] *ASM Handbook, Volume 2: Properties and Selection: Nonferrous Alloys and Special-Purpose Materials*. ASM International, 1990.

[22] A. T. Gaynor and J. K. Guest. Topology optimization considering overhang constraints: eliminating sacrificial support material in additive manufacturing through design. *Structural and Multidisciplinary Optimization*, 54(5): 1157–1172, 2016.

[23] M. Leary, L. Merli, F. Torti, M. Mazur, and M. Brandt. Optimal topology for additive manufacture: a method for enabling additive manufacture of support-free optimal structures. *Materials & Design*, 63:678–690, 2014.

[24] N. Morris, A. Butscher, and F. Iorio. A subtractive manufacturing constraint for level set topology optimization. *Structural and Multidisciplinary Optimization*, 61:1573–1588, 2020.

[25] Matthijs Langelaar. Topology optimization for multi-axis machining. *Computer Methods in Applied Mechanics and Engineering*, 351:226–252, 2019. doi: 10.1016/j.cma.2019.03.037.

[26] Flaviana Calignano, Massimo Lorusso, Jukka Pakkanen, Francesco Trevisan, Elisa P. Ambrosio, Diego Manfredi, and Paolo Fino. Investigation of accuracy and dimensional limits of part produced in aluminum alloy by selective laser melting. *The International Journal of Advanced Manufacturing Technology*, 88(1):451–458, 2017. doi: 10.1007/s00170-016-8788-9.

[27] Floriane Zongo, Antoine Tahan, and Vladimir Brailovski. Scale, material concentration, stress relief and part removal effects on the dimensional behaviour of selected AlSi10Mg components manufactured by laser powder bed fusion. *Journal of Manufacturing and Materials Processing*, 3(2):49, 2019. doi: 10.3390/jmmp3020049.

[28] M. Saravana Kumar, Che-Hua Yang, Muhammad Umar Farooq, V. Kavimani, and Adediran Adeolu Adesoji. Enhanced structural integrity of laser powder bed fusion based AlSi10Mg parts by attaining defect free melt pool formations. *Scientific Reports*, 13:16672, 2023. doi: 10.1038/s41598-023-43718-2.

[29] S. Suresh. *Fatigue of Materials*. Cambridge University Press, Cambridge, 2nd edition, 1998.

[30] R. I. Stephens, A. Fatemi, R. R. Stephens, and H. O. Fuchs. *Metal Fatigue in Engineering*. Wiley-Interscience, New York, 2nd edition, 2001.

[31] I. Maskery, N. T. Aboulkhair, C. Tuck, R. D. Wildman, I. A. Ashcroft, N. M. Everitt, and R. J. M. Hague. Fatigue performance enhancement of selectively laser melted aluminium alloy by heat treatment. In *Proceedings of the 26th Annual International Solid Freeform Fabrication Symposium*, pages 1017–1025, Austin, TX, USA, 2015.

[32] E. Brandl, U. Heckenberger, V. Holzinger, and D. Buchbinder. Additive manufactured AlSi10Mg samples using selective laser melting (SLM): microstructure, high cycle fatigue, and fracture behavior. *Materials and Design*, 34:159–169, 2012.

[33] J. N. Domfang Ngnekou, Y. Nadot, G. Henaff, J. Nicolai, W. H. Kan, J. M. Cairney, and L. Ridosz. Fatigue properties of AlSi10Mg produced by additive layer manufacturing. *International Journal of Fatigue*, 119:160–172, 2019.

[34] Peter Mercelis and Jean-Pierre Kruth. Residual stresses in selective laser sintering and selective laser melting. *Rapid Prototyping Journal*, 12(5):254–265, 2006. doi: 10.1108/13552540610707013.

[35] J. E. Campbell, S. Gao, T. Bennett, J. Dean, and T. W. Clyne. Indentation plastometry: A new approach to extracting stress–strain curves from indentation data. *Advanced Engineering Materials*, 23(5):2001208, 2021. doi: 10.1002/adem.202001208.

[36] Y. T. Tang, J. E. Campbell, M. Burley, J. Dean, R. C. Reed, and T. W. Clyne. Profilometry-based indentation plastometry to obtain stress–strain curves from anisotropic superalloy components made by additive manufacturing. *Materialia*, 15:101017, 2021. doi: 10.1016/j.mtla.2021.101017.

[37] P. Li, Y. Kim, A. C. Bobel, L. G. Hector, A. K. Sachdev, S. Kumar, and A. F. Bower. Microstructural origin of the anisotropic flow stress of laser powder bed fused AlSi10Mg. *Acta Materialia*, 220:117346, 2021. doi: 10.1016/j.actamat.2021.117346.

[38] K. Kempen, L. Thijs, J. Van Humbeeck, and J.-P. Kruth. Mechanical properties of AlSi10Mg produced by selective laser melting. *Physics Procedia*, 39:439–446, 2012.

[39] C. Weiss, C. Boedger, E. Schiefer, D. Heussen, and C. L. Haefner. Evaluation of the ecological footprint for parts from AlSi10Mg manufactured by laser powder bed fusion. In *Solid Freeform Fabrication 2022: Proceedings of the 33rd Annual International Solid Freeform Fabrication Symposium*, page 921, Austin, TX, USA, 2022.

[40] R. Huang, M. Riddle, D. Graziano, J. Warren, S. Das, S. Nimbalkar, J. Cresko, and E. Masanet. Energy and emissions saving potential of additive manufacturing: the case of lightweight aircraft components. *Journal of Cleaner Production*, 2016.

[41] E. Alonso, T. M. Lee, C. Bjelkengren, R. Roth, and R. Kirchain. Evaluating the potential for secondary mass savings in vehicle lightweighting. *Environmental Science & Technology*, 2012.

[42] K. Moawad and A. Mayyas. Battery resizing enabled by vehicle lightweighting: implications for battery-pack manufacturing emissions, cost, and critical mineral demand in battery electric vehicles. *Transportation Engineering*, 24, 2026.

[43] Lorenzo Del Giudice, Rafał Wróbel, Antonios A. Katsamakas, Christian Leinenbach, and Michalis F. Vassiliou. Physical modelling of reinforced concrete at a 1:40 scale using additively manufactured reinforcement cages. *Earthquake Engineering & Structural Dynamics*, 51 (3):537–551, 2022. doi: 10.1002/eqe.3578.

[44] U.S. Geological Survey. Mineral commodity summaries 2025: Aluminum. Technical report, U.S. Geological Survey, Reston, VA, 2025. Accessed: 27 July 2026.

[45] T. Peng, Y. Wang, Y. Zhu, Y. Yang, Y. Yang, and R. Tang. Life cycle assessment of selective-laser-melting-produced hydraulic valve body with integrated design and manufacturing optimization: a cradle-to-gate study. *Additive Manufacturing*, 36, 2020.

[46] D. Böckin and A.-M. Tillman. Environmental assessment of additive manufacturing in the automotive industry. *Journal of Cleaner Production*, 226:977–987, 2019.

[47] J. Faludi, M. Baumers, I. Maskery, and R. Hague. Environmental impacts of selective laser melting: do printers, powder, or power dominate? *Journal of Industrial Ecology*, 21: S144–S156, 2017.

[48] S. Kokare, J. P. Oliveira, T. G. Santos, and R. Godina. Environmental and economic assessment of a steel wall fabricated by wire-based direct energy deposition. *Additive Manufacturing*, 61 (5):1–14, 2023.

[49] D. Landi, F. Colombo Zefinetti, C. Spreafico, and D. Regazzoni. Comparative life cycle assessment of two different manufacturing technologies: laser additive manufacturing and traditional technique. *Procedia CIRP*, 105:700–705, 2022.

A. Vehicle Load Derivation

Table 11 showcases the vehicle data used, and Fig. 14 shows the corresponding free-body diagrams.

Table 11: Vehicle and rear-left upright geometry parameters used in the load derivation of Section 2.

Parameter	Symbol	Value
Vehicle mass and geometry		
Car mass	m_{car}	234.3 kg
Driver mass	m_{driver}	72.35 kg
Total vehicle mass	m	306.7 kg
Wheelbase	L	1.795 m
CoG longitudinal position	x_{CoG}	0.8790 m
CoG height	h	0.3123 m
Front track width	T_f	1.108 m
Rear track width	T_r	1.115 m
Mass distribution		
Static weight distribution, front	$\%_f$	51.02 %
Unsprung mass, front (per corner)	$m_{us,f}$	9.200 kg
Unsprung mass, rear (per corner)	$m_{us,r}$	12.47 kg
Sprung mass	m_s	263.1 kg
Tyre and friction		
Lateral friction coefficient	μ_{lat}	1.200
Rear tyre diameter	—	0.4064 m
Rolling radius, rear	r_R	0.2032 m
Rear-left upright geometry		
Bearing spacing	l_1	35.00 mm
Bearing to wheel-centre offset	l_2	12.00 mm
Calliper radius, vertical	$l_{3,v}$	46.39 mm
Calliper radius, horizontal	$l_{3,h}$	67.91 mm
Calliper mount spacing	l_4	25.27 mm
Calliper mount spacing	l_5	96.00 mm
Calliper mount angle	θ	30.00°

B. Hybrid Reconstruction Method

The hybrid variant of Section 3.10.4 was produced by the procedure below. It is stated in general terms, as it is intended to transfer to any generatively designed component that must ultimately be produced by conventional means.

1. Export the solver outcome as a mesh. The selected outcome, additive or milling-constrained, is exported in a mesh format rather than converted to a boundary-representation solid. This is deliberate. A mesh cannot be dimensioned, filleted or referenced by downstream parametric features, so the solver result cannot be silently merged with, or mistaken for, manufacturable geometry. Its role is restricted to that of a reference, which is what prevents the non-parametric surface problem identified in Section 3.10.2 from propagating into the CAD definition.

2. Import and align on the preserves. The mesh is inserted into the document containing the existing part and the two bodies are aligned on the preserve geometry common to both.

3. Reduce the opacity of the baseline body. With the existing part set to low opacity, the mesh remains visible within the design envelope.

4. Rebuild parametrically from the preserves outward. Modelling begins at the preserve geometries, which are fixed by the assembly and therefore not subject to interpretation.

5. Verify against SF. The reconstructed part is to be analysed in the finite-element model of Section 4 under the identical governing load cases and assessed against the same $SF \geq 1.5$ and $u_{\max} \leq 0.2$ mm criteria used throughout the generative design study (Section 3.5). This is part of future work.

C. Manufacturing Sustainability Analysis: Method and Assumptions

The carbon figures reported in Section 5.6 were produced with Manufacturing Sustainability Insights (MSI), the Autodesk Fusion lifecycle module, using emission factors from Gravity Climate. The system boundary comprises primary raw-material production, inbound transportation and manufacturing process energy, with results expressed as kg CO_2e per component. The assessment is a comparison of manufacturing routes, designs and materials, evaluated for future reference rather than as a certified lifecycle assessment.

Region, grid and material origin. All cases were evaluated within a United Kingdom manufacturing region, so a UK grid carbon intensity is applied to process energy throughout. The raw material originates from China, which produces well over half of the world's primary aluminium [44], and is shipped from Shanghai to a representative UK destination. Post-processing is excluded across all processes, as are the use and end-of-life phases, since no representative study is currently available. Material classes such as Al 6061 and AlSi10Mg are assigned the same raw-material factor despite differing production routes.

Additive (LPBF) feedstock and processing. Feedstock conversion for LPBF involves gas atomisation of the metal ingot into powder, with Gravity Climate using values from the stainless-steel study of Peng *et al.* [45], also employed by Böckin and Tillman

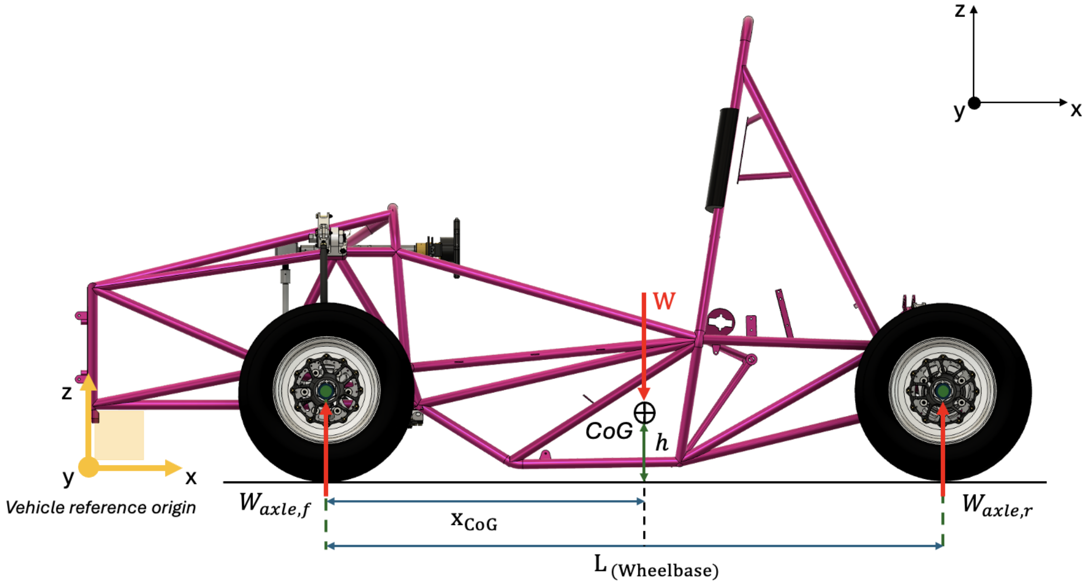

Figure 14: Free-body diagrams of the vehicle at static equilibrium, referenced from Section 2.2. W is the total static weight (Eq. 1); $W_{\text{axle},f}$ and $W_{\text{axle},r}$ are the front and rear axle loads

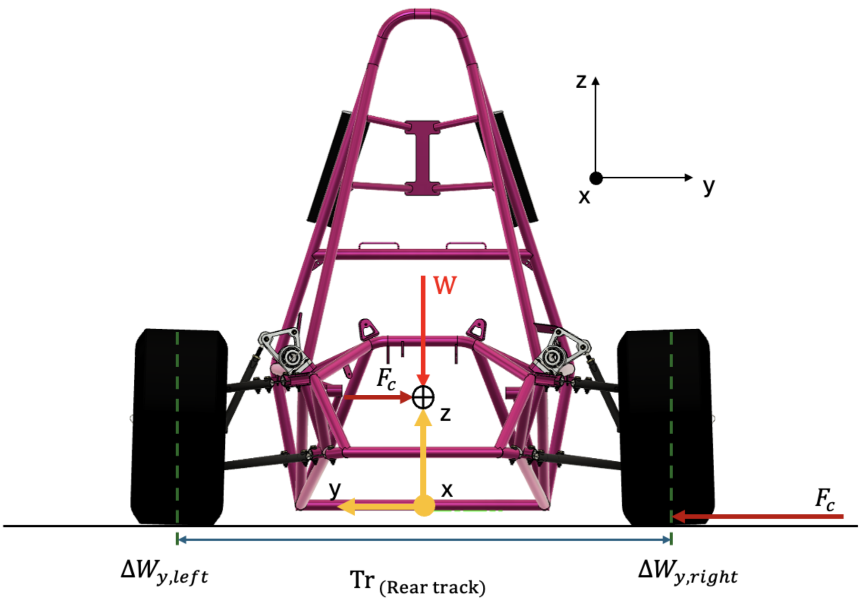

Figure 15: Free-body diagram of the corresponding per-wheel value $W_{\text{wheel},f}$, $W_{\text{wheel},r}$ of Eq. 2, under the lateral-symmetry assumption stated there. h, x_{CoG} and L are the centre-of-gravity height, its longitudinal position, and the wheelbase, listed in Table 10. This static split is the baseline from which the longitudinal and lateral load-transfer terms of Section 2.3 are derived.

[46], which incorporates both UK grid-specific electrical energy and inert-gas consumption. Argon is assumed to escape entirely to atmosphere rather than being recovered, as acknowledged by Faludi *et al.* [47]. Manufacturing process factors are expressed as raw specific energy consumption rather than as carbon per unit mass, enabling application of a UK grid intensity derived from the mean of eight lifecycle assessments compiled by Böckin and Tillman [46], with the underlying dispersion detailed by Kokare *et al.* [48].

Subtractive (milling) feedstock and processing. For milling, energy for raw-material extraction and transport is based on a rectangular billet with 10 mm added to each face of the component's bounding box.

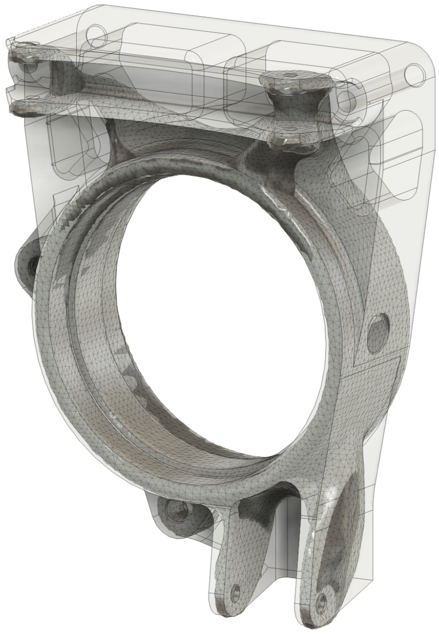

Figure 16: Hybrid reconstruction of the rear-left upright: solver outcome imported as a mesh.

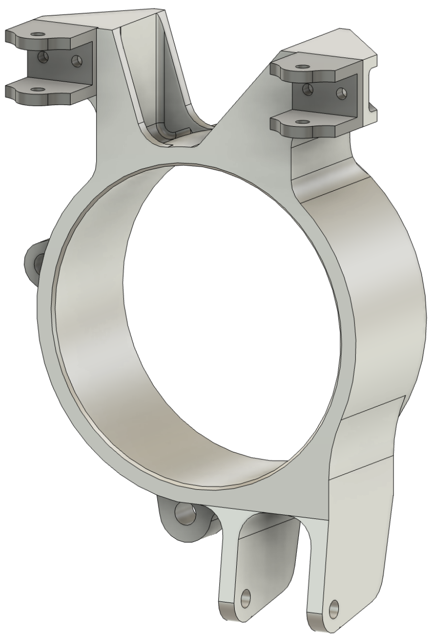

Figure 17: Hybrid reconstruction of the rear-left upright: parametric reconstruction, 810 g.

The equivalent conversion term is the casting energy modelled by Landi *et al.* [49], noting that it varies across alloys and part geometries.

Emissions accounting. Total carbon emissions are the sum of transport, raw material (production of the raw metal) and processing. For LPBF, processing comprises metal atomisation, process energy consumption and material loss; for CNC milling, it comprises casting, process energy and material loss.

D. Fatigue Material Data

The S–N data used in Section 4.3.3 was derived from the as-built LPBF AlSi10Mg fatigue study of Maskery *et al.* [31]. That work publishes its fatigue results graphically; the only numerical S–N information is the Basquin fit, for which the as-built parameters are $\log(A) = 2.86 \pm 0.09$ and $B = -0.21 \pm 0.02$ at a load ratio of $R = 0.1$. Stress amplitudes were reconstructed from these parameters and converted to fully-reversed equivalents by the Goodman relation using the as-built ultimate tensile strength of 330 MPa reported in the same study. The reconstruction was verified against the source: evaluation at 10^6 cycles returns a maximum stress of 88.5 MPa against the 85 MPa fatigue strength quoted at that life.

Table 12: Derived S–N dataset as entered into ANSYS Engineering Data.

N_f (cycles)	S_a **at** $R = 0.1$ (MPa)	S_m (MPa)	$S_{a,eq}$ **at** $R = -1$ (MPa)
1×10^4	104.7	128.0	171.1
2×10^4	90.5	110.7	136.2
5×10^4	74.7	91.3	103.2
1×10^5	64.6	78.9	84.9
2×10^5	55.8	68.2	70.4
5×10^5	46.0	56.3	55.5
1×10^6	39.8	48.7	46.7
2×10^6	34.4	42.0	39.5
5×10^6	28.4	34.7	31.7
1×10^7	24.6	30.0	27.0
3×10^7	19.5	23.8	21.0

Table 13: Fatigue Tool configuration.

Setting	**Value**
Analysis type	Stress life
Loading type	Ratio
Mean stress theory	Goodman
Stress component	Equivalent (von Mises)
Fatigue strength factor	$K_f = 1$
Scale factor	1
Interpolation	Log–log

E. Manufactured Part Observations

Two mirrored builds were produced from the same GD outcome on the same LPBF system to the same parameter set (Section 5.3.2). Build 1 was bead-blasted, 192.7 g against a CAD reference of 196.88 g (2.12 % lighter). Build 2 was supplied in the as-built condition with adhered powder retained, accounting for the difference in surface colour and texture in Fig. 18 rather than any underlying build difference; at 188.7 g against the same CAD reference, it is 4.15 % lighter. Build 2 also exhibited a concentrated deformation at the brake calliper mounting boss (Fig. 19). The affected bore is a mounting interface: this bounds the finding to assembly fit rather than to the reported safety factors, which do not depend on this feature (Section 6.2).

Figure 18: Mirrored LPBF builds and the calliper-mount deformation observed on Build 2: Build 1 (left, bead-blasted) and mirrored Build 2 (right, as-built).

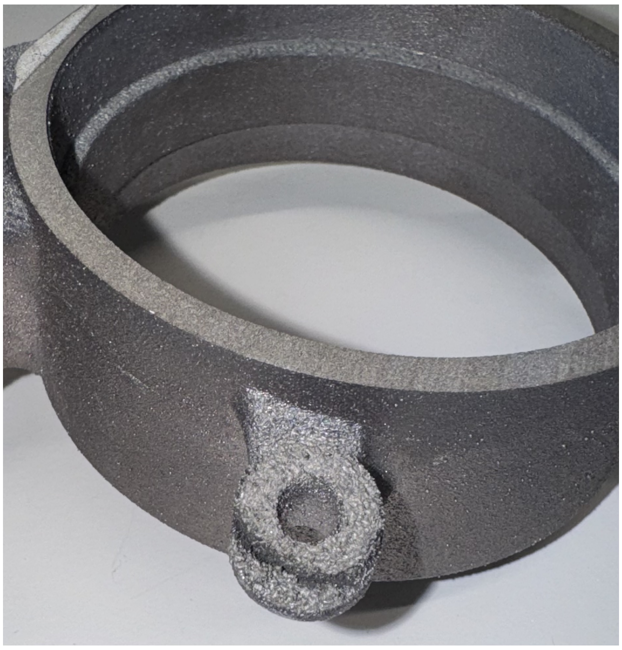

Figure 19: Mirrored LPBF builds and the calliper-mount deformation observed on Build 2: close-up of Build 2's calliper mounting boss.

F. Physical Validation Test Rig

Physical validation of the finite-element model was planned through a sponsorship agreement with Procter and Chester Measurements (PCM), established after the initial project scope was set and therefore carried here as future work. The AlSi10Mg build will first undergo rigorous post-processing to reach the surface finish required for reliable strain gauging (Ra 0.2). PCM will then professionally support the following: the design of bespoke loading fixtures that reproduce realistic suspension load paths within a uniaxial test frame; the installation of three-element strain-gauge rosettes at the predicted stress hotspots, resolving both the magnitude and direction of the principal stresses; and instrumented loading of the part, correlating the measured strains against the FEA predictions to quantify how closely the simulation matches physical behaviour.

Loading condition. The test frame is designed to reproduce the corner-entry pushrod reaction of 9084 N derived in Section 2.7 (Table 1), the single largest member force acting on the upright under the governing load cases. Rather than applying this force along an arbitrary axis, the fixture is oriented to match the pushrod's own load line: resolved into the vehicle reference frame of Fig. 1, the reaction is $\mathbf{F} = (673, \ -3922.90, \ -8166)$ N, corresponding to 26.0° off vertical, or 64.0° above the testing bed (Fig. 20). Matching the fixture angle to the pushrod's load line, rather than testing under a simplified vertical or horizontal load, ensures the strain state recovered at the gauges reflects the same combined bending and axial loading the component experiences in service, rather than a decomposed or idealised approximation of it.

Gauge placement. Consistent with the peak stress concentration identified under both governing load cases (Section 5.1, Fig. 12), the rosettes are positioned at the lower clevis, where the upper and lower wishbone legs and the pushrod converge. The corner-entry condition combined with a kerb strike reaches a peak equivalent stress of 98.79 MPa at this joint (Table 7, regime 6), distributed asymmetrically between the two clevis legs (Fig. 21); gauges are placed on both legs rather than the single node tracked in the fatigue assessment of Section 4.3.3, so the physical test can confirm which leg governs rather than assuming the modelled one does.

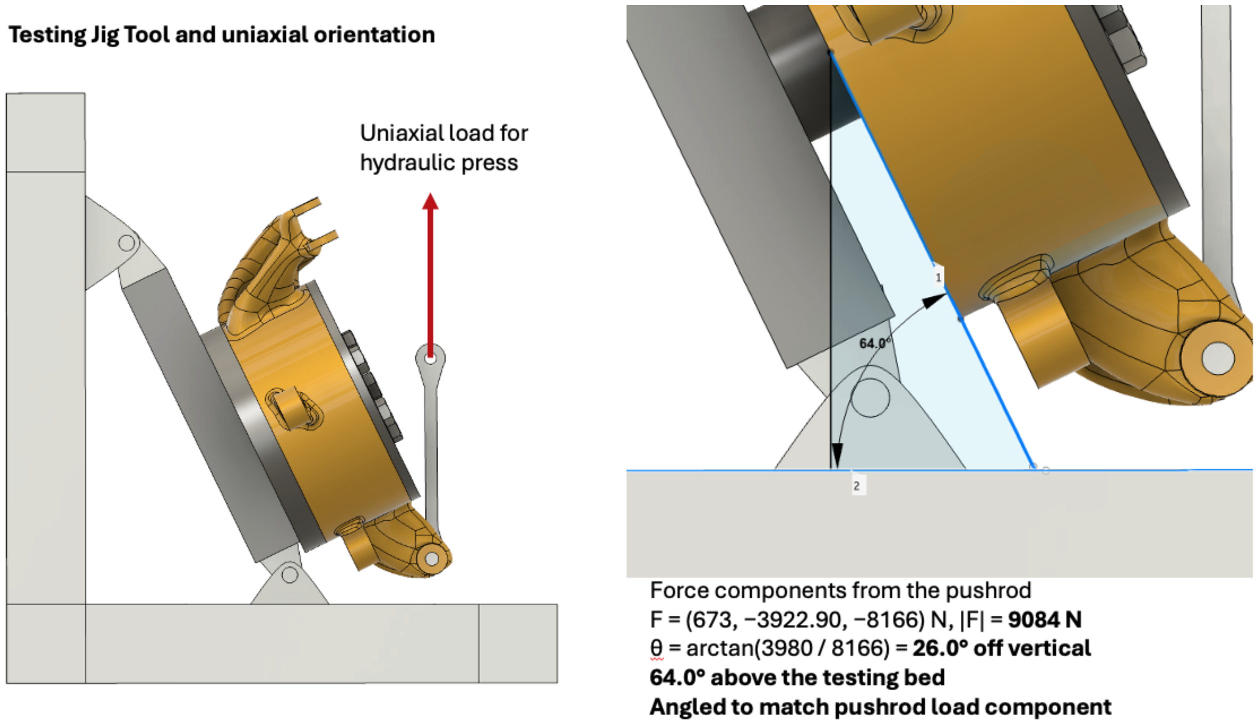

Figure 20: Proposed uniaxial test jig, oriented to reproduce the corner-entry pushrod load line. Force components resolved in the vehicle reference frame of Fig. 1; magnitude and orientation derived from the pushrod reaction of Table 1.

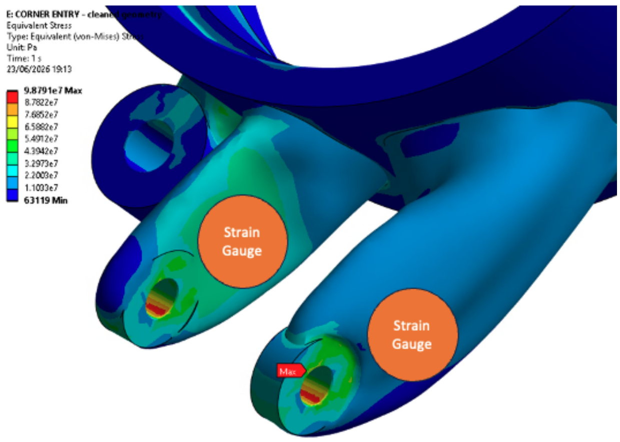

Figure 21: Corner-entry (with kerb strike) equivalent stress contour, showing the proposed strain-gauge rosette locations at the two lower clevis legs. Peak equivalent stress 98.79 MPa, corresponding to duty-cycle regime 6 of Table 7.

The correlation between measured and predicted strain at these two locations, evaluated against the governing corner-entry condition, would provide the first physical check on the finite-element model validating the safety factor reported in this thesis.